

LEWIS GRANT
IN-07-CR
99262
P.65

Dale E. Van Zante
Theodore H. Okiishi
December 1991

(NASA-CR-190433) VISUALIZATION OF
BOUNDARY-LAYER DEVELOPMENT ON TURBOMACHINE
BLADES WITH LIQUID CRYSTALS Final Technical
Report (Iowa State Univ. of Science and
Technology) 65 p

N92-27519

63/07 Unclas
0099262

Visualization of Boundary-Layer Development on Turbomachine Blades with Liquid Crystals

TURBOMACHINERY
COMPONENTS RESEARCH PROGRAM

Final Technical Report
NASA Grant NAG 3-917

***Visualization of Boundary-Layer
Development on Turbomachine Blades
with Liquid Crystals***

Dale E. Van Zante
Theodore H. Okiishi

Department of Mechanical Engineering
Iowa State University

December 1991

ISU-ERI-Ames-92114
TCRL-36
ERI Project 3067



**engineering
research institute**
iowa state university

TABLE OF CONTENTS

	Page
LIST OF TABLES	iii
LIST OF FIGURES	iv
ABSTRACT	vi
ACKNOWLEDGEMENTS	vii
1. INTRODUCTION	1
2. LIQUID CRYSTALS	3
3. LINEAR CASCADE	15
4. BOUNDARY-LAYER VISUALIZATION USING TEMPERATURE SENSITIVE LIQUID CRYSTALS	20
4.1. Hot-film Gage Results	20
4.2. Blade Surface Temperature Distribution	22
4.3. Boundary-Layer Development Visualization	25
4.4. $Re = 330,000$, $Tu = 0.8\%$ Case	26
4.5. $Re = 700,000$, $Tu = 6.4\%$ Case	32
5. BOUNDARY-LAYER VISUALIZATION USING SHEAR SENSITIVE LIQUID CRYSTALS	39
6. CONCLUSIONS	52
REFERENCES	55

LIST OF TABLES

Table 3.1. Turbine cascade geometric parameters.	15
Table 3.2. Test Reynolds numbers and corresponding cascade inlet velocities.	17

LIST OF FIGURES

Fig. 2.1.	Smectic liquid crystal structure.	5
Fig. 2.2.	Nematic liquid crystal structure.	5
Fig. 2.3.	Structure of cholesteric or chiral nematic liquid crystals.	6
Fig. 2.4.	Reflection coefficient for a hypothetical liquid crystal with a 500-nm reflective wavelength.	8
Fig. 2.5.	Effects of temperature on pitch length.	9
	a. Helix length change with temperature.	9
	b. Displacement angle change with temperature.	9
Fig. 2.6.	Color response versus temperature of temperature-sensitive liquid crystals.	10
Fig. 2.7.	Boundary-layer transition on a Learjet wing using liquid crystals ($M = 0.8$, $h = 48,000$ ft).	12
Fig. 2.8.	Liquid crystal pattern at zero angle of attack.	14
Fig. 2.9.	Film injection cooling of a cylinder in crossflow.	14
Fig. 3.1.	Blade geometry and coordinate system.	16
Fig. 3.2.	Cascade wind tunnel.	16
Fig. 3.3.	Hot-film gage use on the suction surface.	18
Fig. 4.1.	Selected AC voltage waveforms for $Re = 330,000$ and $Tu = 0.8\%$.	21
Fig. 4.2.	AC voltage waveforms along suction surface for $Re = 330,000$ and $Tu = 0.8\%$.	23
Fig. 4.3.	DC and RMS voltage output from hot-film sensors for $Re = 330,000$ and $Tu = 0.8\%$.	24
Fig. 4.4.	Results from the $Re = 330,000$, $Tu = 0.8\%$ test.	27
	a. Trailing edge.	27
	b. Leading edge.	30
Fig. 4.5.	Selected AC voltage waveforms for $Re = 700,000$ and $Tu = 6.4\%$.	33
Fig. 4.6.	DC and RMS voltage output from hot-film sensors for $Re = 700,000$ and $Tu = 6.4\%$.	33
Fig. 4.7.	Results from the $Re = 700,000$ $Tu = 6.4\%$ case.	35
	a. Trailing edge.	35
	b. Leading edge.	37
Fig. 5.1.	Color response of shear sensitive crystals on blade surface with no endwall suction.	40

Fig. 5.2.	Focal-conic and Grandjean liquid crystal textures.	42
Fig. 5.3.	Crystals on the blade surface in the focal-conic texture.	44
Fig. 5.4.	DC and RMS voltage output from hot-film sensors for $Re = 540,000$ and $Tu = 0.8\%$ case.	44
Fig. 5.5.	Flow-induced color change showing turbulent reattachment and turbulent flow region.	45
	a. No endwall suction.	45
	b. With endwall suction.	45
Fig. 5.6.	Permanent color change due to flow-induced texture change from focal conic to Grandjean.	46
	a. No endwall suction.	46
	b. With endwall suction.	46
Fig. 5.7.	Crystals on the blade surface in the Grandjean texture.	48
Fig. 5.8.	Brushing the crystals to obtain Grandjean texture.	48
Fig. 5.9.	Turbulent reattachment showing as shear-induced color change in the crystals .	49
	a. No endwall suction.	49
	b. With endwall suction.	49
Fig. 5.10.	Crystals in Grandjean texture after a test (no airflow).	50
	a. No endwall suction.	50
	b. With endwall suction.	50

ABSTRACT

This report documents a study of the use of liquid crystals to visualize boundary-layer development on a turbomachine blade. A turbine blade model in a linear cascade of blades was used for the tests involved. Details of the boundary-layer development on the suction surface of the turbine blade model were known from previous research. Temperature sensitive and shear sensitive liquid crystals were tried as visualization agents. A foil heater powered electrically was flush mounted on the turbine blade surface as a necessary component during the temperature sensitive liquid crystal tests. Auxiliary components were not used with the shear sensitive liquid crystals. The temperature sensitive crystals were very effective in their ability to display the location of boundary-layer flow separation and reattachment. Visualization of natural transition from laminar to turbulent boundary-layer flow with the temperature sensitive crystals was possible but subtle. The visualization of separated flow reattachment with the shear sensitive crystals was easily accomplished when the crystals were allowed to make a transition from the focal-conic to a Grandjean texture. Visualization of flow reattachment based on the selective reflection properties of shear sensitive crystals was achieved only marginally because of the larger surface shear stress and shear stress gradient levels required for more dramatic color differences.

ACKNOWLEDGMENTS

The work described in this report was accomplished in the Iowa State University Mechanical Engineering Department Turbomachinery Components Research Laboratory under National Aeronautics and Space Administration Grant NAG 3-917. This sponsorship is gratefully acknowledged. We appreciate very much the encouragement we received from the grant technical monitor, Dr. Michael D. Hathaway of the U.S. Army Aviation Systems Command Propulsion Directorate at the NASA Lewis Research Center.

We gained much from the technical assistance we received from laboratory colleagues, Mark Kroneman, Dr. Zhuanglin Zhang, and David Halstead. Their own research and suggestions were very helpful.

We thank Dr. Michael Parsley of Hallcrest for his help in obtaining the variety of liquid crystals that we used. We are also grateful to Marcia Pierson and Kurt Plagge of the Office of Editorial Services for their work in making this report available.

1. INTRODUCTION

Surface boundary layers on turbomachine blades are an important design consideration. The extent of laminar, transitional, turbulent and separated boundary-layer flow regions on a turbomachine blade largely determines the aerodynamic performance of that blade. However, boundary-layer transition and flow separation on turbomachine blade are not yet well understood, this being especially true when blade row interaction effects are involved.

As examples of the significant influence of blade boundary-layer development on a turbomachine performance, two examples are cited. Hodson [1] compared the aerodynamic performance of an axial-flow turbine rotor blade section in a turbine stage and in a linear cascade. The measured profile loss of the blade section was 50% higher in the stage than in the cascade. He attributed this difference in performance to the influence of nozzle blade wakes on rotor blade boundary-layer development. Batson and Okiishi [2] compared computer code-predicted losses with measured losses for two transonic fan stage stators and concluded that the computed extent of the transition region and location of flow separation influenced predicted loss values appreciably relative to measured losses.

Laminar, transitional, and turbulent boundary-layer flows on turbomachine blades have been sensed in the past with surface hot-film gages. For example, with several individual surface hot-film gages, Dring et al. [3] were able to detect Tollmien Schlichting waves and subsequent turbulent flow on the suction surface of an axial-flow turbine stator blade. Hodson [4] used an array of hot-film sensors to confirm relaminarization of the boundary layer on the suction surface of a high-speed turbine blade section. Hansen and Okiishi [5] used several hot-film gages to detect boundary-layer behavior on the suction and pressure surfaces of an axial-flow compressor stator blade. Other documented means for detecting boundary-layer transition on turbomachine blades include surface flow visualization [6] and boundary-layer flow measurements with a hot-wire probe [7, 8].

Separated flows on turbomachine blades have been detected with surface hot-film gages [9, 10, 11], surface pressure taps [12], surface flow visualization [11, 13, 14], and a laser-doppler velocimeter [15].

Halstead, Okiishi, and Wisler [16] recently employed a novel, sliding surface hot-film gage to document details of boundary-layer development, including transition and the formation of a small separation bubble on a turbine blade model in a linear cascade.

As explained in Refs. [17] and [18], liquid crystal coatings have also been successfully used recently to make visible the location of boundary-layer transition and flow separation on a

variety of aircraft-related surfaces (e.g. wing sections, winglets, engine nacelles, and a fuselage forebody). Both flight and wind tunnel tests were performed.

Chiral nematic and cholesteric liquid crystals involve a molecular pattern that is helical [17, 18]. The pitch length of the molecular pattern is altered in response to changes in temperature, shear stress level, or both, and different helix pitch lengths result in variations of the color of the liquid crystal coating [17, 18]. The specific color observed is dependent on the local shear stress, temperature, or both, and the intensity of the reflected colors depends on the amount and angle of the incident light [18].

The intent of this report is to document the results of a study on the use of liquid crystal coatings to visualize boundary-layer development on a turbomachine blade surface. A turbine blade model set in a linear cascade was selected for this work because the boundary-layer development on the suction surface of this blade was already well known [16].

2. LIQUID CRYSTALS

The recorded history of liquid crystals began around 1850 when some European scientists observed the interesting optical behavior of certain liquids when they were viewed under polarized light. Liquids normally do not exhibit any optical behavior when viewed under polarized light. The scientists noted their observations but did not realize they were viewing another state of matter. Credit for the "discovery" of liquid crystals is generally given to Austrian botanist Friedrich Reinitzer [19]. In 1888 he noticed that a compound of cholesterol displayed unusual phase change behavior during the transition from a crystalline solid to an isotropic liquid. When heated above the temperature at which the crystalline lattice is stable, the solid compound melted forming a cloudy liquid. At a higher temperature the cloudy liquid turned clear. Reinitzer proposed that this cloudy liquid might be another phase of matter. Because he posed the correct questions for future investigators, Reinitzer is usually called the "discoverer" of liquid crystals. Reinitzer sent samples of the compound to another researcher, Otto Lehmann. Lehmann found that this intermediate cloudy phase, or mesophase, contained regions that had a crystal-like molecular structure. He suggested the name "liquid crystal". Even though there is an apparent contradiction in this nomenclature, the name has prevailed. Lehmann went on to become the dominant figure in liquid crystal research around the turn of this century.

Liquid crystals are more like liquids than solids. Thermodynamically, more energy is required for the solid to liquid crystal transition than for the liquid crystal to isotropic liquid transition. Molecules of solids have positional as well as orientational order. When a solid melts, both types of order are lost. The molecules of a liquid have no specific orientation or position within the liquid. When a solid melts into a liquid crystal, however, some of the orientational order is retained. The average orientation of the molecules is described by a director r . This small amount of additional order gives liquid crystals some unique physical properties. Some liquid crystals respond to temperature changes, mechanical stress (tangential or shear and normal or pressure), chemical environment, or electric and magnetic fields. Some exhibit the selective reflection of light, or changing colors as it appears to the human eye. Liquid crystals that are temperature sensitive and liquid crystals that are shear sensitive were used in this study.

Liquid crystals are classified by their structure and optical properties. From differing optical properties three classes are distinguished; smectic, nematic, and cholesteric (chiral nematic). The term cholesteric is not a good one because many cholesteric liquid crystals have no connection with cholesterol whatsoever. The more proper term is chiral nematic that indicates a twisted nematic phase. Then by structure it can be argued that only two basic classes exist, smectic and

nematic. The cholesteric (chiral nematic) class is a special case of nematic. Structural class is identified by the packing arrangement of the long cigar-shaped liquid crystal molecules. Liquid crystals formed of disk-shaped molecules also exist but will not be discussed here. The smectic crystal structure is shown in Fig. 2.1 from Ref. [20]. Smectic crystals have their molecules arranged so that their long molecular axes are parallel. In addition to this molecular alignment, the molecules are arrayed in two-dimensional sheets one molecule thick. In some smectic liquid crystals the molecules have a specific packing arrangement within the layers. Figure 2.1 suggests a random molecular arrangement within each layer. Smectic liquid crystals are the most ordered form of liquid crystals.

The nematic liquid crystal structure is less ordered than the smectic. Nematic crystals have their long molecular axes parallel, but they are not separated into layers. The nematic structure is shown in Fig. 2.2 from Ref. [20]. Both smectic and nematic liquid crystals exhibit many of the same optical properties as solid crystals.

The liquid crystals used in this study were special formulations of nematic crystals, namely, chiral nematic crystals that are classified separately from other nematics because they exhibit unusual optical activity which is caused by their naturally twisted molecular structure. As shown in Fig. 2.3 from Ref. [21], each planar layer of molecules involves molecule axes that are aligned. Here r gives the direction of axes alignment. Each layer must have the axes of the molecules twisted from the previous layer to accommodate molecular side groups extending out of the molecular plane of an essentially flat molecule. On a multilayer scale the director traces out a helix in space. This helix leads to the unusual optical activity of the chiral nematic crystals.

When an electromagnetic wave passes through a material, the charges in the material also emit electromagnetic waves. Because the material is uniform in its electric or magnetic properties in all directions, the waves tend to cancel except for those traveling in the same direction as the original wave. However, if the electric or magnetic properties are not uniform but repeat over a distance equal to half the wavelength of the wave, an important phenomenon occurs. Because of the half wavelength spacing, each wave traveling in the backward direction emerges from the material in phase. The waves add together instead of cancelling and constructive interference occurs. This means that a large electromagnetic wave is not only transmitted but is reflected also.

Liquid crystals are optically active substances. Constructive interference occurs in chiral nematic liquid crystals when the wavelength of the light (electromagnetic wave) is equal to the pitch length of the crystals. If white light, which is a mixture of wavelengths, is incident on chiral nematic crystals, most of the light will pass through except for light of the specific wavelength

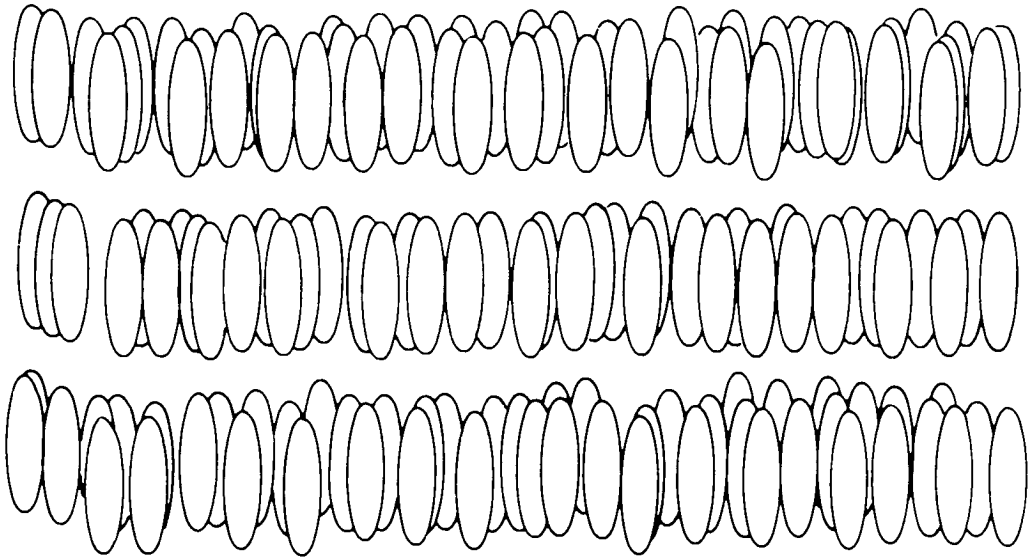


Figure 2.1. Smectic liquid crystal structure.

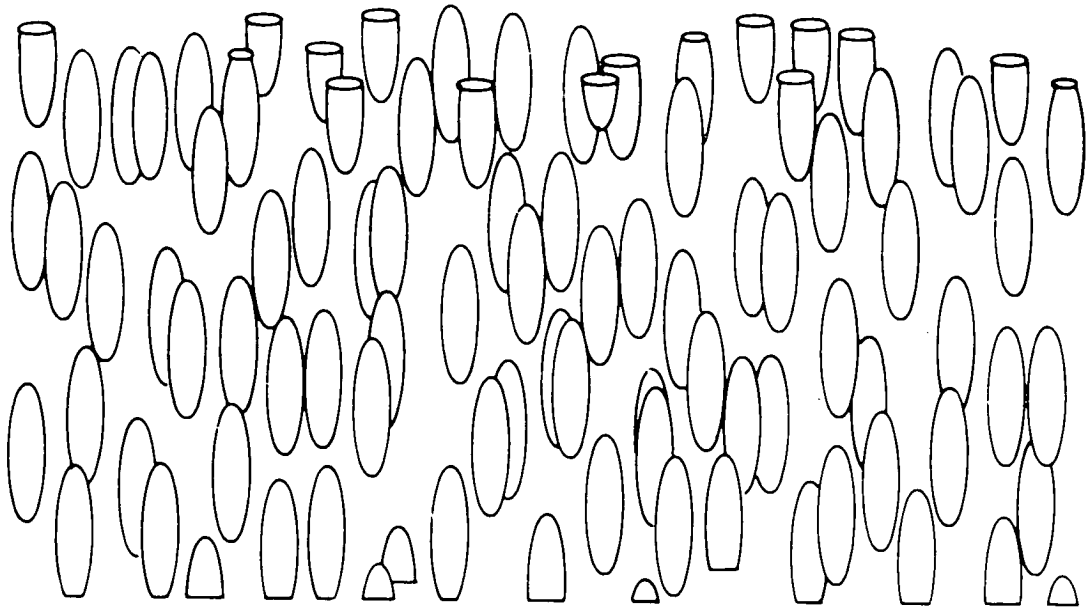


Figure 2.2. Nematic liquid crystal structure.

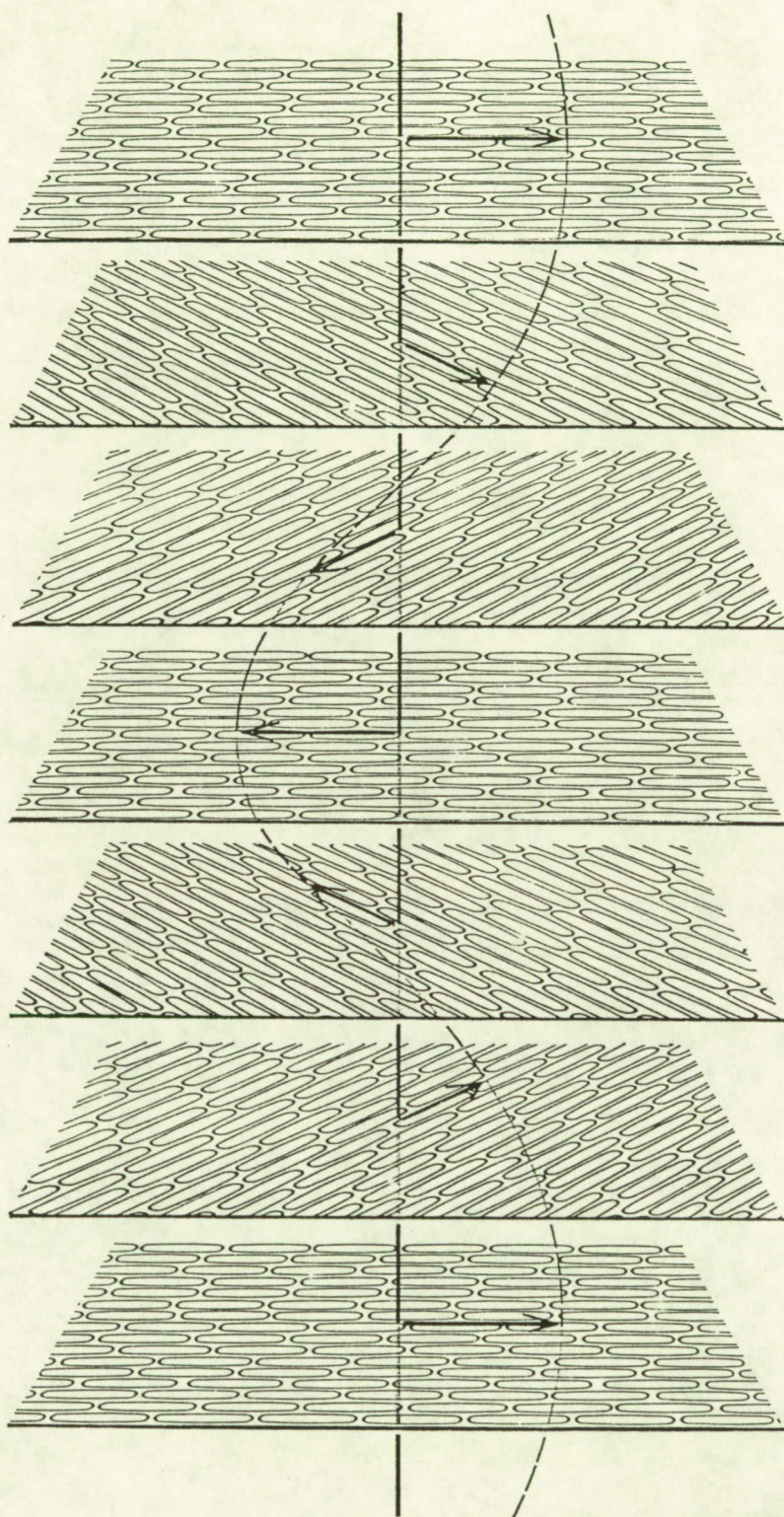


Figure 2.3. Structure of cholesteric or chiral nematic liquid crystals.

equal to the crystal pitch. This phenomenon is called selective reflection since only one wavelength is reflected. If this wavelength is in the visible spectrum, it will be seen as a bright pure color.

Figure 2.4 from Ref. [20] shows the reflection coefficient of a hypothetical liquid crystal with a 500 nm reflective wavelength. As the wavelength approaches 500 nm, the reflectivity increases rapidly; at 500 nm the reflectivity is 100%. The narrow band of high reflection coefficient causes the colors to appear very pure. Only a small portion of the incident light is reflected; therefore the crystals should be viewed against a dark nonreflecting background which absorbs the transmitted light.

The reflected color depends on the pitch length of the liquid crystals. Pitch length is the distance through the crystal layers in which the director rotates 360° . As pitch length changes due to temperature or mechanical stress change, the wavelength and thus the color of the reflected light changes. Pitch length decreases as the liquid crystal's temperature is increased, causing light of shorter wavelengths to be reflected.

The pitch length varies by two mechanisms. Consider a temperature rise. First, the intermolecular distances along the helix lengthens, which increases the pitch length. Secondly, the displacement angle between adjacent layers of molecules increases, which decreases the pitch length. The two effects are shown in Fig. 2.5 from Ref. [20]. In chiral nematic compounds the net effect of the two mechanisms is that pitch length decreases as temperature increases. Changes in displacement angle dominate helix length changes. Very small changes in displacement angle cause the reflected light color to scan the entire visible spectrum.

Temperature-sensitive liquid crystals (TLCs) are described by their red start temperature and bandwidth. Figure 2.6 from Ref. [20] shows the color versus crystal temperature response of TLCs used in this study. At a lower temperature the crystals appear colorless because the wavelengths of the reflected light are in the infrared range. As the crystal temperature is gradually increased the crystals will first appear red in the visible spectrum. The red start temperature is the temperature for which the crystals first appear red. As the crystal temperature is increased further above the red start temperature, the color play changes from red to yellow to green to blue to violet. Finally, when the temperature is high enough, the crystals reflect in wavelengths from violet to ultra-violet which appear colorless. The range in temperatures between the red start temperature and the crystals appearing blue is called the bandwidth. All of the visible color play of the crystals occurs within the bandwidth. Crystals can be formulated in many different red start bandwidth combinations.

Reflection Coefficient

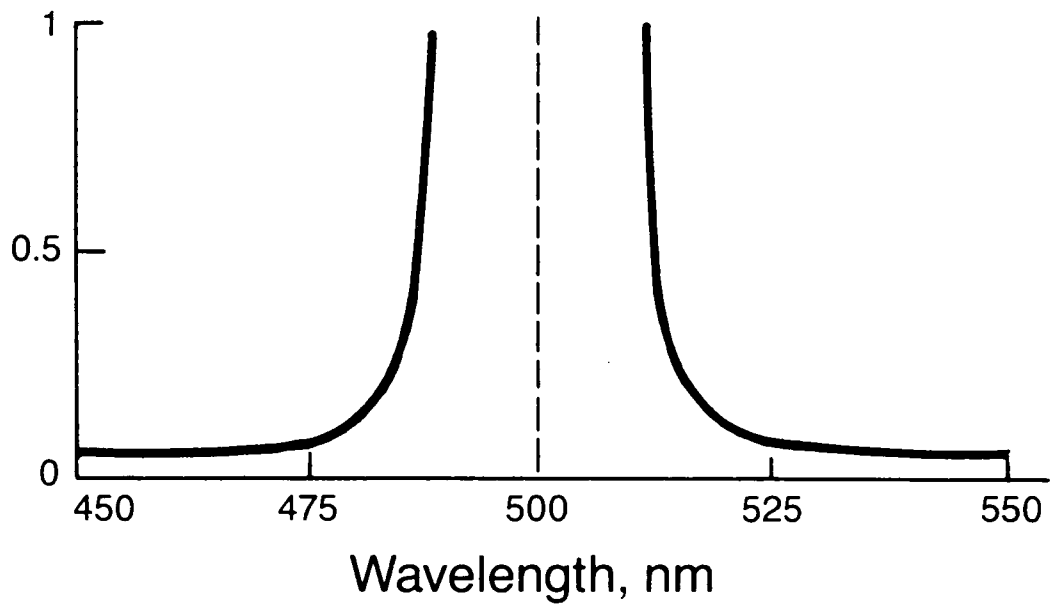
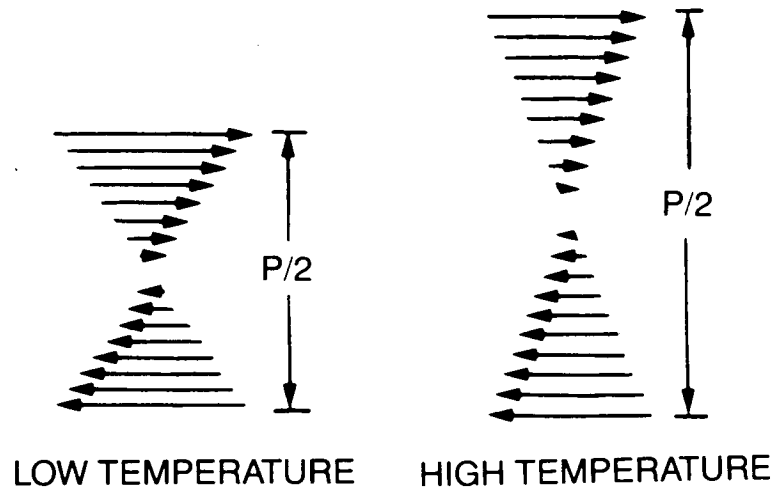
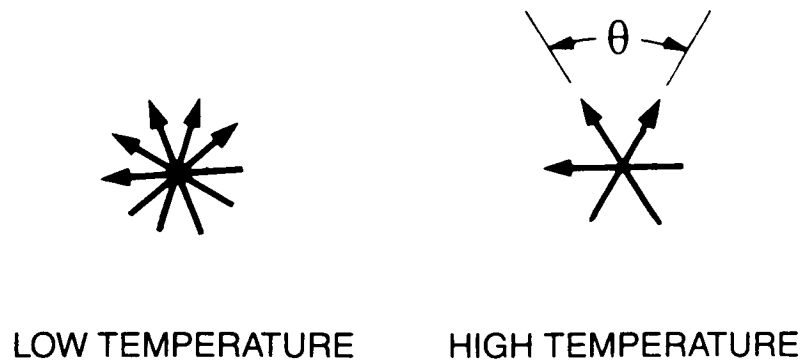


Figure 2.4. Reflection coefficient for a hypothetical liquid crystal with a 500-nm reflective wavelength.



a. Helix length change with temperature.



b. Displacement angle change with temperature.

Figure 2.5. Effects of temperature on pitch length.

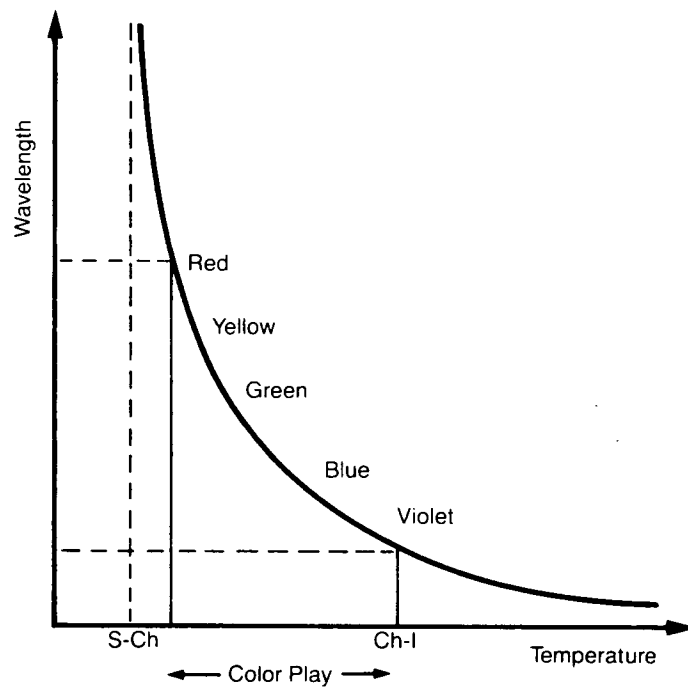


Figure 2.6. Color response versus temperature of temperature-sensitive liquid crystals.

Commercially available temperature-sensitive liquid crystals are identified by a code. This code normally specifies a red start temperature (R); the temperature scale used, Celsius (C) or Fahrenheit (F); and the bandwidth (W). For example, a temperature-sensitive liquid crystal with a red start temperature of 30° C and a 1° C bandwidth would be identified as R30C1W. Shear sensitive crystals are identified by a code that specifies the crystal type, chiral nematic (CN) for example, and the clearing point temperature, e.g., R45C. After application on a surface, the shear sensitive crystals are normally a deep red color. The clearing point temperature is the temperature at which the crystals appear colorless, 45° C for the example given. The complete code might look like CN/R45C. The codes used will vary depending on the manufacturer. The examples given are the most common forms.

Liquid crystals are available in an encapsulated form and as unencapsulated or neat liquid crystals. Neat liquid crystals are the compounds in a raw chemical form. Their appearance varies from clear liquids to an opalescent grease. Neat liquid crystals are normally dissolved in a solvent for mixing and application. Shear sensitive crystals need direct exposure to their environment so they are always supplied in the neat or unencapsulated form.

Microscopic droplets of liquid crystal are enclosed in a polymer shell to produce the encapsulated form of the liquid crystals. This process is used primarily for temperature sensitive liquid crystals. The gelatin coating protects the liquid crystals from the degrading effects of oxygen and ultraviolet light. The encapsulated crystals can be mixed with a binder to form a sprayable paint coating. The encapsulated crystals can also be applied to a sheet of mylar. A coat of nonreflective black paint backs the crystals to form a prefabricated liquid crystal sheet. Neat crystals, encapsulated crystals, and prefabricated sheets were all used in our tests.

Even though liquid crystals and their optical properties were discovered before the turn of the century, they were not used in aerodynamic applications until the late 1960s. The crystals were initially used in their raw or neat form because microencapsulation had not yet been developed. Liquid crystals were first used in supersonic flow by Klein [22] who used chiral nematic crystals to observe boundary-layer development on a flat plate at $M_\infty = 1.62$ and a wing-body model at $M_\infty = 1.98$. Quantitative surface temperature measurements were also attempted on a flat plate at $M_\infty = 3.0$ by using the liquid crystals. These preliminary investigations proved a potential for the methods.

Klein and Margozzi [23] attempted to measure skin friction coefficient with liquid crystals and had only limited success. This was attributed to the running of the crystals due to aerodynamic shear and the difficulty in separating temperature, viewing angle, and pressure effects from shear effects.

ORIGINAL PAGE
COLOR PHOTOGRAPH

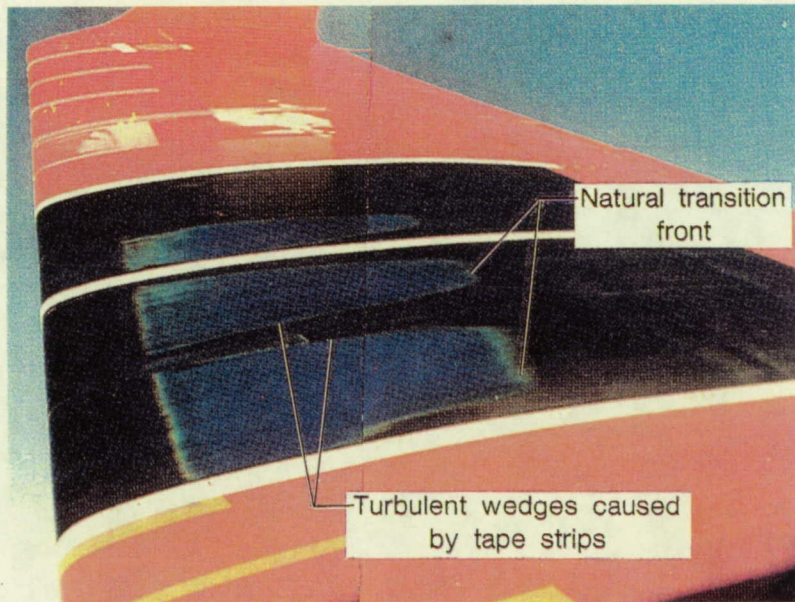


Figure 2.7. Boundary-layer transition on a Learjet wing using liquid crystals
($M = 0.8$, $h = 48,000$ ft).

More recently, Holmes and Obara [18] extended the use of liquid crystals to subsonic and transonic applications in flight and in wind tunnels. Transition was successfully observed on aircraft wings under a variety of conditions. Figure 2.7 from Ref. [18] shows liquid crystals being used to observe boundary-layer transition on a Learjet wing. The liquid crystals used were sensitive to temperature and shear stress. The range and brightness of the color play produced was a combination of both shear and temperature effects.

In early studies, care was taken to set the event (red start) temperature equal to the anticipated test surface temperature so the liquid crystal coating could show color play in response to shear. Advances in liquid crystal formulations made since the late 60s have allowed the development of shear sensitive crystals that have almost no sensitivity to temperature changes. Reda [24] used these advanced crystals to observe the unsteady effects of a dynamic stall process on an oscillating airfoil. An example of his liquid crystal response is shown in Fig. 2.8 from Ref. [24]. The crystals appear red when applied to the blade. Under the shear load the crystals appear yellow. These higher shear regions are the yellow-colored areas on the leading and trailing edges of the blade. Near the midspan the flow is separated and at this location the crystals remain red because of the low shear inside the separation region.

The development of microencapsulation allowed liquid crystals to respond with bright colors to temperature changes with protection from the degrading effects of oxygen and ultraviolet light and the elimination of any shear effects. The encapsulated crystals also made possible other application methods such as sprayable coatings and prefabricated sheets.

Hippensteele, Russell, and Stepka [25] evaluated the use of a composite of a liquid crystal sheet and a heating element to study the heat-transfer performance of turbine blade cooling designs. An example of the application of their technique to evaluation of film cooling on a cylinder is illustrated in Fig. 2.9 from Ref. [25]. Note that the film cooling is only effective in a small region directly downstream from the injection holes. Local heat-transfer coefficients were determined by using the procedure and equipment developed. Hippensteele, Russell, and Torres [26] again used the liquid crystal-heater composite to determine heat-transfer coefficients along the midspan portion of a five times scale turbine blade model in a linear cascade. These results were compared with analytical values calculated from the STAN5 boundary-layer code. High-resolution heat-transfer coefficients were determined by Hippensteele, Russell, and Torres [27] on a turbine airfoil with turbulence and surface roughness effects. Jones and Hippensteele [28] extended their liquid crystal evaluation methods from turbine blade models to compound curved surfaces with transient heat-transfer conditions.

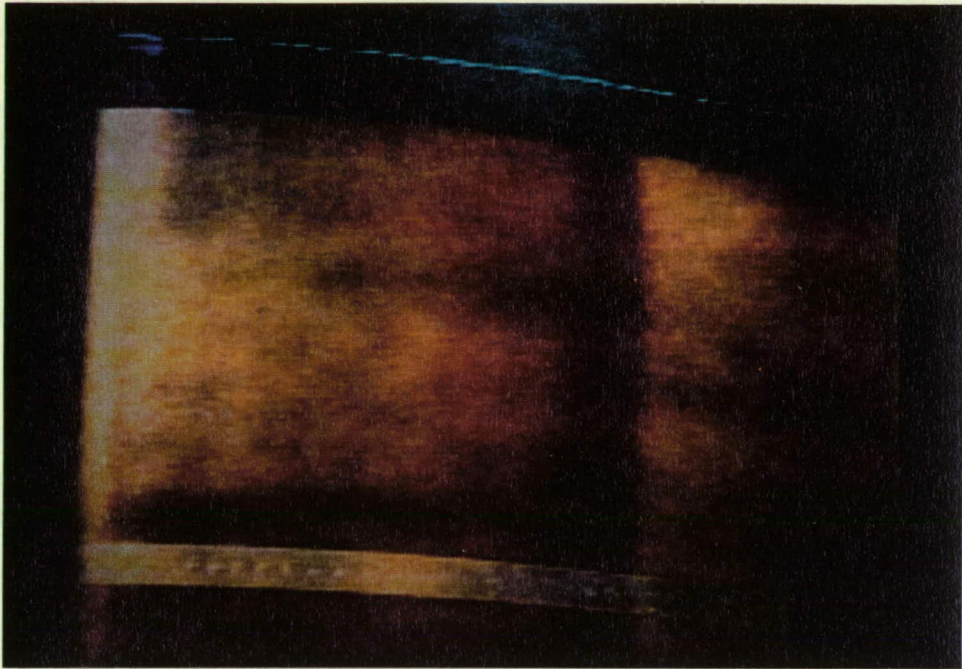


Figure 2.8. Liquid crystal pattern at zero angle of attack.

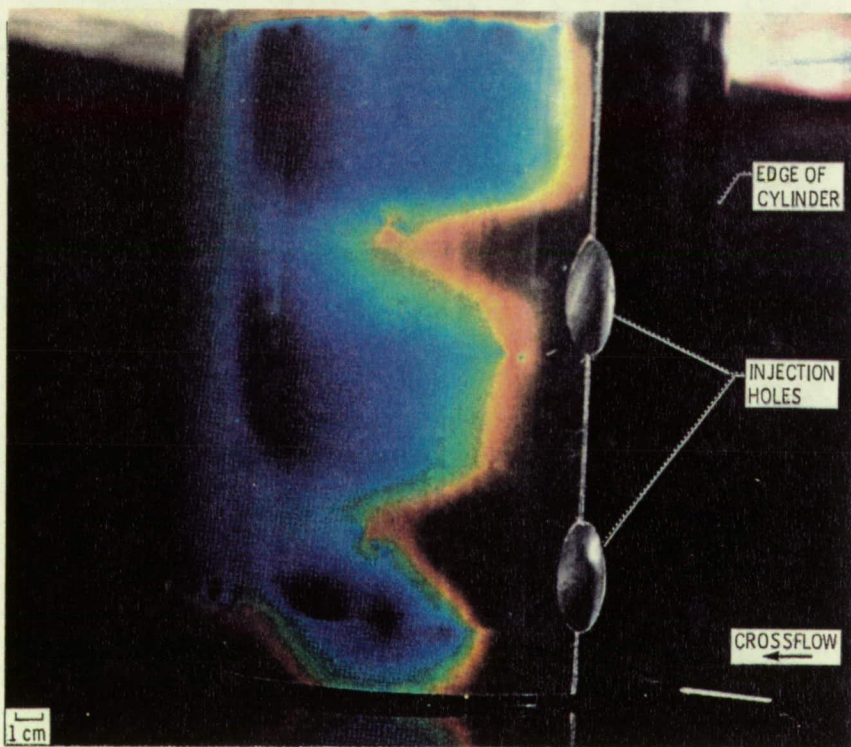


Figure 2.9. Film injection cooling of a cylinder in crossflow.

3. LINEAR CASCADE

The linear cascade of turbine blade models designed by Vijayaraghavan and Kavanagh [11] was used for the liquid crystal boundary-layer development visualization tests. The cascade pack consisted of five identical airfoils secured with Plexiglass upper and lower endwalls. Endwall boundary-layer suction was available. The airfoils were constructed out of mahogany wood. Each airfoil had a span length of 10.0 inches and an axial chord length of 8.0 inches to yield an aspect ratio of 1.25. The airfoil geometry and coordinate nomenclature are illustrated in Fig. 3.1. Airfoil geometry details are summarized in Table 3.1.

Table 3.1. Turbine cascade geometric parameters.

Axial chord, B_x (in.)	8.0
Leading edge radius, R_{LE} (in.)	0.56
Trailing edge radius, R_{TE} (in.)	0.24
Pitch-axial chord ratio, $\frac{\tau}{B_x}$	1.12
Throat-pitch ratio, $\frac{\lambda}{\tau}$	0.4067
Leading edge blade angle, β_1^* (deg from axial)	52.0
Trailing edge blade angle, β_2^* (deg from axial)	-66.3
Stagger angle, γ (deg from axial)	-33.0
Uncovered turning angle, Γ (deg)	17.0

The cascade wind tunnel is shown in Fig. 3.2. The airflow through the cascade was provided by a Buffalo Forge blower with a 200 horsepower electric motor and a variable speed drive. Air was routed from the blower through a 30-in. diameter piping system. The flow entered a plenum box where the flow was straightened and the turbulence level adjusted by use of different grids. A 3.3:1 two-dimensional contraction followed the plenum box and routed the flow into the cascade pack. Flow periodicity across the cascade was achieved by properly adjusting the sidewalls and tailboards.

The cascade operating condition was varied to yield different airfoil-surface boundary-layer development patterns. The cascade inlet turbulence intensity level and the airfoil chord Reynolds number (based on axial chord length and exit velocity) could be changed. A turbulence intensity of

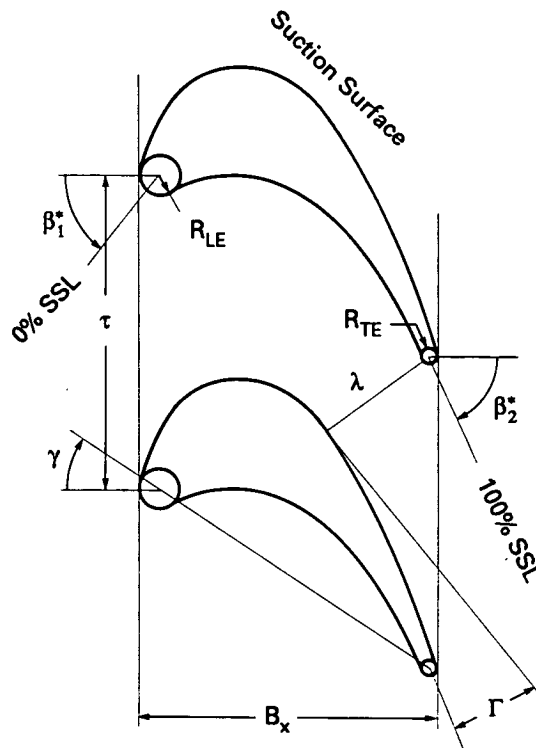


Figure 3.1. Blade geometry and coordinate system.

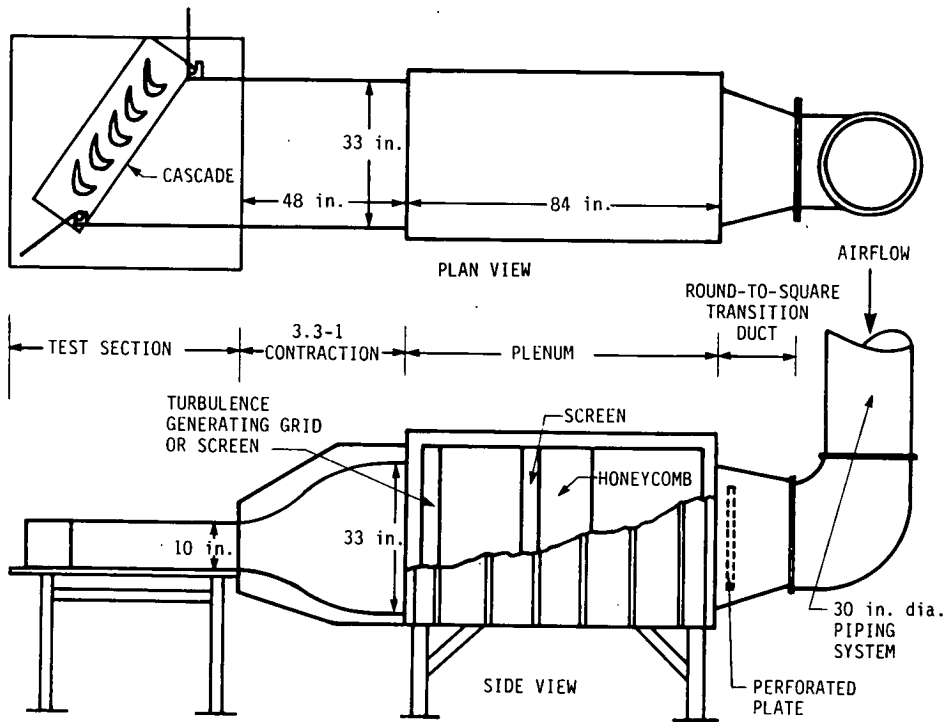


Figure 3.2. Cascade wind tunnel.

0.8% was achieved with a fine wire screen upstream of the contraction section. A larger turbulence intensity level of 6.4% was made available for tests by replacing the screen with a coarse grid of wooden slats. The generated turbulence was established as being homogeneous [11]. For all tests, the airflow entered the cascade at a design inlet angle, β_1 , of 45 deg (-7 deg incidence). The cascade inlet velocity levels associated with the test Reynolds numbers are summarized in Table 3.2. The velocity level was changed by varying the speed of the blower motor.

Table 3.2. Test Reynolds numbers and corresponding cascade inlet velocities.

Reynolds Number	Cascade Inlet Velocity (ft/s)
700,000	100.0
540,000	77.1
330,000	47.1

A sliding surface hot-film gage was used by Halstead, Okiishi and Wisler [16] as indicated in Fig. 3.3 to ascertain the status of the boundary layer on the suction surface of the test airfoil.

For the temperature-sensitive liquid crystal studies, an inconel foil heater was attached to the test airfoil surface. The inconel was alloy IN600 annealed 0.001 inch foil available through Teledyne Rodney Metals. Originally the foil heater covered the entire suction surface of the blade. However, imperfections in the blade model surface caused the foil to wrinkle during application. The wrinkling problem was reduced by applying the foil to the midspan portion of the blade only. The foil was cut to the desired width and to a length adequate to cover the suction side of the blade with several inches of overlap onto the blade pressure surface. The inconel foil wrinkled very easily and required handling with extreme care. For the best results, the foil was bonded to the blade surface before attaching copper bus bars for the electrical connections.

An aggressive double-sided adhesive sheet was used to mount the foil to the blade surface. Hallcrest recommended Mactac SB 1786 that is a mylar-based adhesive sheet. We used a paper-based adhesive sheet that is normally used for mounting photographs. The adhesive sheet was first applied to the blade surface with care taken to remove any air bubbles from underneath the sheet. The inconel foil was then applied to the adhesive surface with extreme care to prevent wrinkles in

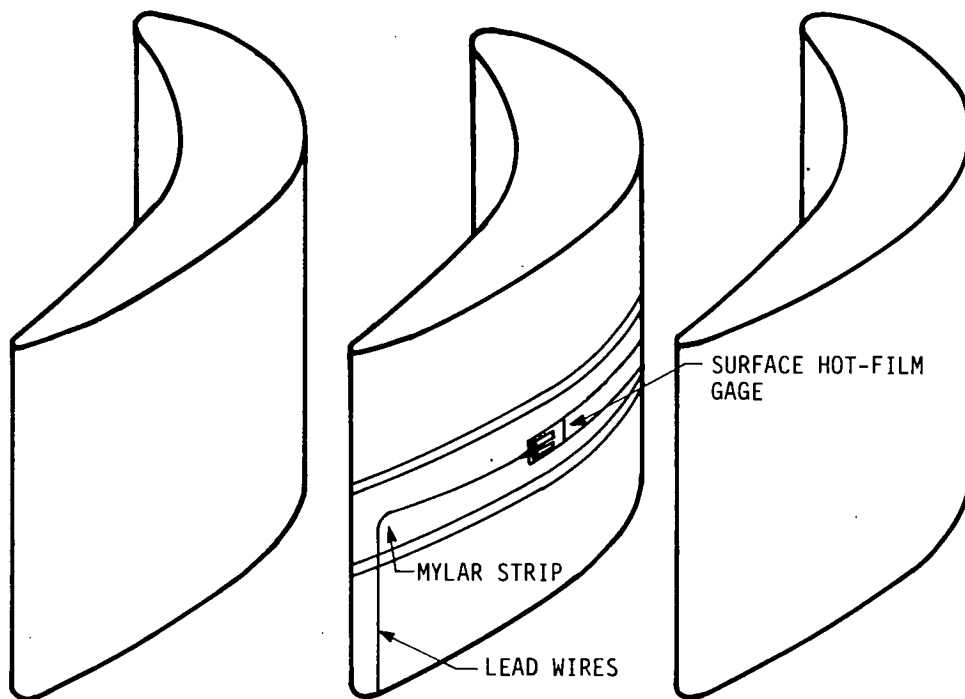


Figure 3.3. Hot-film gage use on the suction surface.

the foil sheet and air bubbles trapped beneath the foil sheet. The excess amount of foil wrapped around to the blade pressure surface was left unbonded so that the bus bars could be attached.

Two copper bus bars, approximately 0.375 in. wide by 0.020 in. thick, were spot welded to each end of the foil sheet. The bus bars were polished with steel wool or sandpaper. The foil sheet was sandwiched between two of the bus bars and this assembly was spot welded at about 0.375 in. intervals along the length of the bus bars. This process was done at both ends of the foil to provide good mechanical and electrical connections between the bus bars and the inconel foil. Wire leads were soldered to the bus bars to provide connection to a low-voltage, high-current power supply. The electrical current required by the heater at test conditions ranged from 10 to 25 amperes at approximately 4.0 v DC. The bus bars and lead wires were attached securely to the pressure surface of the blade.

The temperature-sensitive liquid crystals were applied to the inconel foil surface as sprayable coatings and as prefabricated sheets. Before applying a sprayable coating, the foil surface was painted with a water-based, nonreflective black paint. The crystal coating was then sprayed onto the painted surface. The prefabricated sheets were adhesive backed and were applied directly to the foil surface.

For the shear sensitive crystals, a strip of mylar film wide enough to cover the midspan portion of the blade and long enough to wrap around to the pressure surface was painted with a flat, black, water-based paint. The raw liquid crystals were dissolved in a 1,1,2-Trichlorotrifluoroethane solvent and brushed onto the painted surface. The mylar film with the crystal coating was stretched tightly across the suction surface of the blade and held in place by taping the ends to the pressure surface of the blade.

4. BOUNDARY-LAYER VISUALIZATION USING TEMPERATURE-SENSITIVE LIQUID CRYSTALS

Temperature-sensitive liquid crystals or thermochromic liquid crystals, as their name implies, reflect light at specific frequencies depending on the crystal temperature. In the visible spectrum, this results in color dependence on temperature. A technique was developed to use the color dependence on temperature of these crystals to map the development of boundary-layer flow on the surface of a turbine blade section in a linear cascade of blades. Detailed information about the boundary-layer development on the blade in the cascade was obtained by Halstead, Okiishi, and Wisler [16] using surface mounted hot-film gages. This information provided the basis for matching liquid crystal coloration with boundary-layer development. An electrically powered Inconel foil heater was mounted flush on the blade section with the liquid crystals applied to the foil surface. When a heat flux was produced, the varying surface heat-transfer rate resulted in a surface temperature distribution and thus color variation that could be related to the boundary-layer development on the blade surface.

4.1. Hot-film Gage Results

A prerequisite to understanding how the temperature-sensitive liquid crystals were used to observe boundary-layer development is knowledge of Halstead, Okiishi, and Wisler's [16] hot-film data. They presented their results as AC and RMS output voltage ratios that indicate the unsteadiness of the flow, and DC output voltage ratios that are related to the average amount of local heat transfer from the gage.

Figure 4.1 from Ref. [16] shows selected AC voltage waveforms for the $Re = 330,000$, $Tu = 0.8\%$ case studied by Halstead, Okiishi, and Wisler [16]. The occurrence and location of the separation bubble shown in the figure were verified by using surface flow visualization with a bright pigment/oil coating. For each waveform the first number indicates sensor location as percent suction surface length. The second number is an identification number for each sensor location. Waveforms 1, 10, and 23 show no unsteadiness and indicate a laminar boundary layer. Near the boundary layer separation location at sensor 25, very distinct flow oscillations were detected. The unsteadiness increased greatly within the separation bubble. Turbulent reattachment of the boundary layer occurred at 56% suction surface length (SSL), sensor 31; and the flow remained turbulent from there to the trailing edge of the blade section.

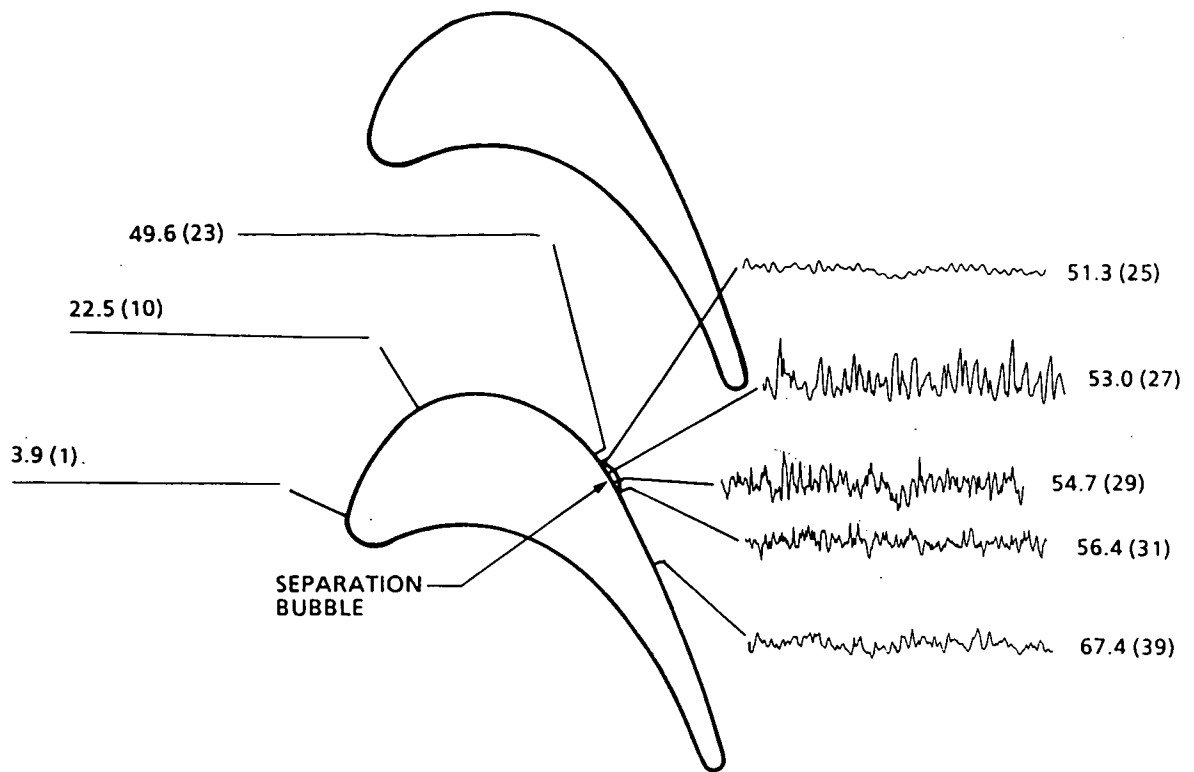


Figure 4.1. Selected AC voltage waveforms for $Re = 330,000$ and $Tu = 0.8\%$.

Figure 4.2 from Ref. [16] shows the complete array of AC voltage waveforms for the $Re = 330,000$ and $Tu = 0.8\%$ case. Note the steadiness of the waveforms to about 50% SSL. Large fluctuations occurred in the separation bubble because of the transition from laminar to turbulent flow that took place over the bubble. The unsteadiness in flow remained from the reattachment location to the trailing edge of the blade indicating turbulent reattachment.

In Fig. 4.3 from Ref. [16], the RMS voltage ratios are very low for boundary-layer flow over 0% to 50% of SSL, indicating laminar flow there. From 50% to 56% SSL, the RMS voltage ratios rise sharply, indicating a flow separation bubble, at this location on the blade surface. The RMS voltage ratios are higher following the separation bubble, indicating a turbulent flow reattachment.

In this example, the DC voltage ratio data suggest local maxima at 23% SSL and 57% SSL. There is also a well-defined local minimum at 51% SSL. This widely varying heat-transfer rate from the gage along the blade surface provided the basis for applying the temperature sensitive liquid crystal method to this flow situation.

4.2. Blade Surface Temperature Distribution

The inconel foil heater was mounted flush on the blade surface to provide an approximately even heat flux on the blade surface. An energy balance of the blade [27] gives:

$$Q_e - Q_l = hA(T_s - T_\infty) \quad (4.1)$$

where Q_e represents the total power input to the heater. The total power minus any losses, Q_l is the convective heat transfer from the blade surface. If $Q_e - Q_l$ is constant along the blade surface, the surface temperature T_s will vary inversely with the local heat-transfer coefficient h .

Hippensteele, Russell, and Torres [26] extensively tested their heater material, vapor-deposited gold-film on polyester sheeting, and determined its uniformity to be $\pm 6\%$. Because of its physical properties, the inconel foil was expected to be more uniform than the $\pm 6\%$ measured for the gold-film. For the current study, the heat flux from the heater Q_e was considered uniform with location on the blade.

The losses Q_l consisted of conduction through the blade material and radiation from the blade surface. Hippensteele, Russell, and Torres [26] found that for their blade cascade arrangement, radiation was negligible and conduction through the blade material was the most significant loss. A qualitative estimate of these losses was obtained by powering the heater with no

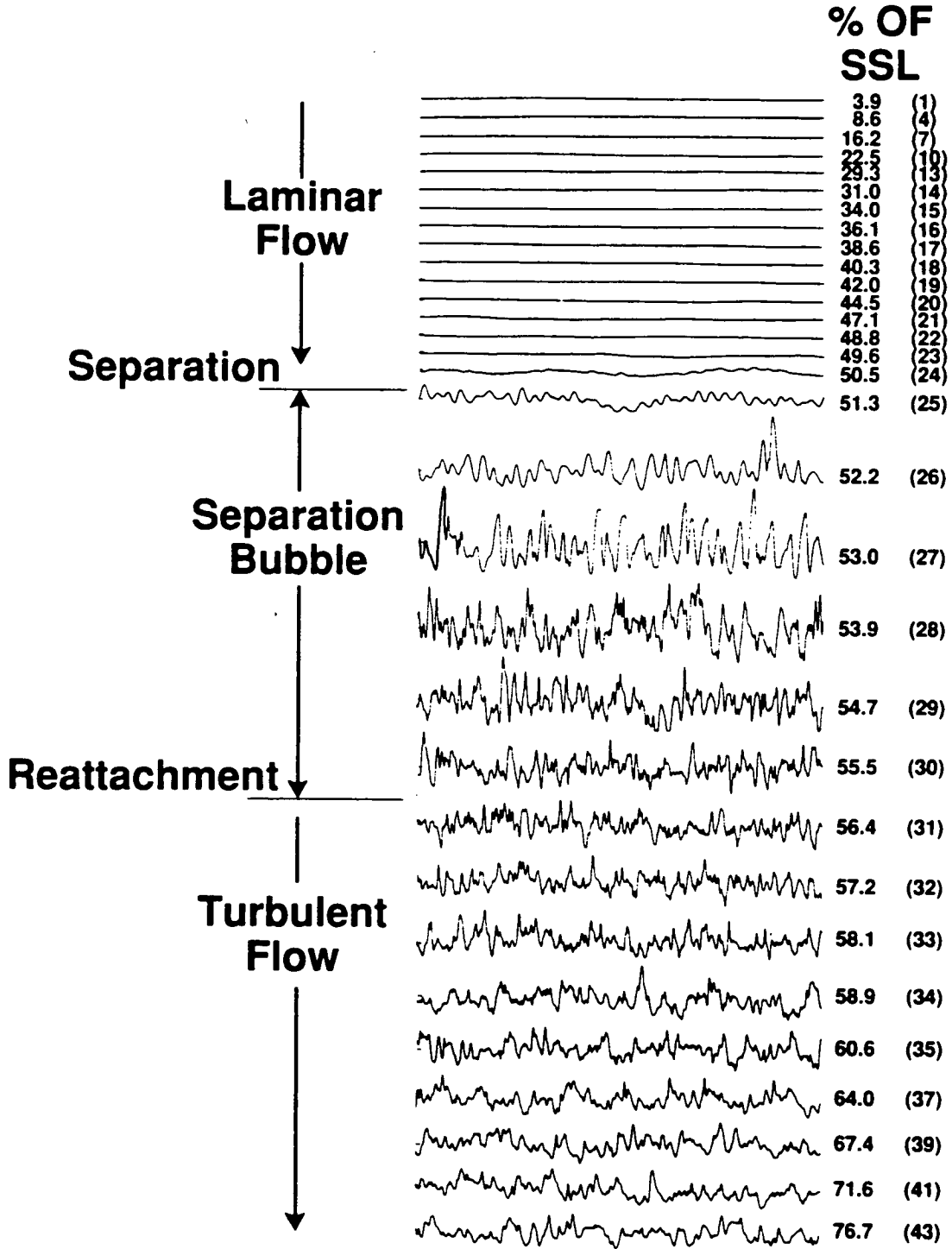


Figure 4.2. AC voltage waveforms along suction surface for $Re = 330,000$ and $Tu = 0.8\%$.

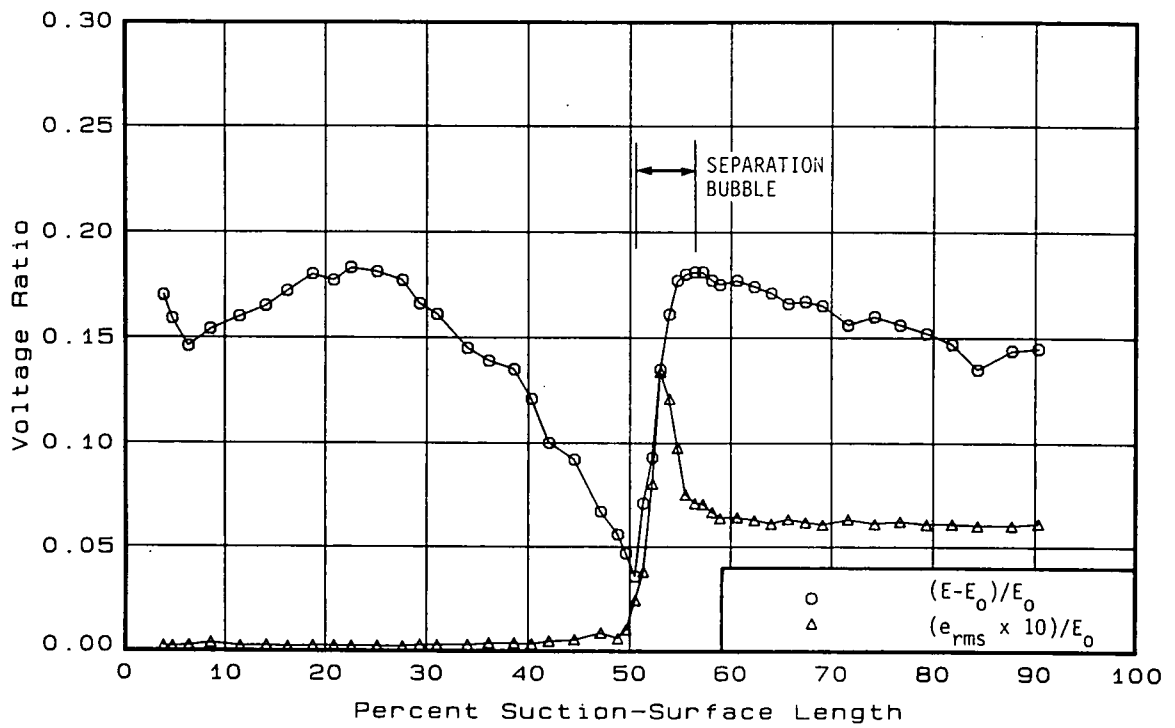


Figure 4.3. DC and RMS voltage output from hot-film sensors for $Re = 330,000$ and $Tu = 0.8\%$.

flow around the blade and observing the liquid crystal coating for color uniformity. For the ISU turbine airfoil, the blade warms first at the trailing edge and 40% - 50% SSL. The effect of this initial temperature distribution, caused by nonuniform losses across the blade surface, on the test observations was not known exactly but was estimated to be negligible. For the qualitative observations done, Q_1 , was not considered. The heat flux due to forced convection, $Q_e - Q_1$ was considered approximately uniform over the blade surface.

With this approximate uniform distribution of heat flux, there was a specific temperature depending on the local heat-transfer coefficient at any point on the blade surface. Because of the varying heat-transfer coefficients on the blade suction surface, there was also a variation of surface temperature along the blade surface.

The hot-film DC voltage ratio curve of Fig. 4.3 from Ref. [16] was used as an approximate indication of the surface temperature distribution on the blade. The highest surface temperature occurred at the point of lowest heat-transfer rate, about 51% SSL in this example. The lowest surface temperatures occurred where the local heat-transfer rates were the highest. Thus by inverting the DC voltage ratio curve, a qualitative surface temperature distribution curve was obtained for the blade section being tested. Changing the level of electrical power to the inconel foil heater changed the range of blade surface temperatures, more electrical power resulting in higher temperatures and vice versa.

4.3. Boundary-layer Development Visualization

A particular surface temperature corresponded to a specific color seen in the crystals. A temperature gradient was made visible by the width of the color bands in the crystals. A rapid change in temperature with distance showed as sharp narrow bands of color. Qualitative comparisons of dT/dx were easily done with the TLCs. However, the response of the crystals is not linear with temperature as suggested by the curve of Fig. 2.6. Yellow is a difficult color to see and is usually a narrow band compared to green or blue. Violet did not appear in the formulations we used. For any quantitative measurements the TLCs must be calibrated first.

To obtain reasonable results, we had to view only a section of the test blade temperature curve at a time. A narrow bandwidth TLC formulation was used, 1°C . At the beginning of the test, we started the airflow and set the heater power low enough so that no color was visible on the blade, i.e., only infrared reflection from the crystals occurred. The visible color play band of the crystals was like a stationary horizontal band of color at temperatures higher than the peak of the low-power, blade-surface-temperature curve. The lower edge of the color play band was red,

corresponding to the red start temperature. The upper edge of the color play band was blue and the other liquid crystal colors were in the midsection of the band. Increasing or decreasing the heater power moved the blade temperature curve up or down relative to the color band. As the heater power was increased from the low-power condition at the start of the test, the blade temperature curve moved upward. The peak of the blade temperature curve eventually "touched" the lower edge of the color play band, and that area of the blade became visible as a red color region. As the heater power was increased further, the blade temperature curve moved further up. The colors seen on the blade surface then corresponded to the intersection of the temperature curve with the visible color play band. The peak of the temperature curve moved into the yellow to green region as the slopes to either side of the peak turn red. Eventually the heater power was increased enough that the temperature peak was above the color band and thus in the colorless region again. The entire blade temperature curve was mapped this way by "moving" the curve through the color play region. A steep slope in the temperature curve showed as narrow color bands as the curve "sliced" through several color bands in a short distance (%SSL). A gradual slope in the temperature curve resulted in wider color bands over the blade surface.

4.4. $Re = 330,000$, $Tu = 0.8\%$ Case

The most dramatic case of boundary-layer flow separation on the test blade occurred at the condition $Re = 330,000$ and $Tu = 0.8\%$. Figure 4.3 from Ref. [16] shows Halstead's hot-film sensor data for these conditions. The RMS voltage ratio data are at a low level from 0% to 50% SSL and indicate laminar flow on this part of the blade surface. The flow remained laminar until the beginning of the separation bubble at 51% SSL. There is a high narrow spike in the RMS voltage ratio data due to high levels of unsteadiness in the bubble. At the trailing edge of the bubble the curve stabilized at a higher voltage ratio and indicated turbulent flow reattachment. The DC voltage ratio data go through a local maximum and decrease at a moderate rate until reaching a minimum at the start of the separation bubble. The DC voltage ratio rises extremely rapidly through the separation bubble and reaches the second local maximum at the end of the bubble at 56% SSL. The DC voltage ratio data then decrease gradually to the trailing edge of the blade. The large rapid change in the DC voltage signal ratio or heat-transfer rate through the separation bubble was easily seen by using the liquid crystals.

Tests were performed by using a Hallcrest spray-on coating of liquid crystals with the formulation R30C 1W. Figure 4.4 shows a series of photographs from a test run taken at discrete power settings. Photo 1 shows the region of initial color on the blade with the narrow red band

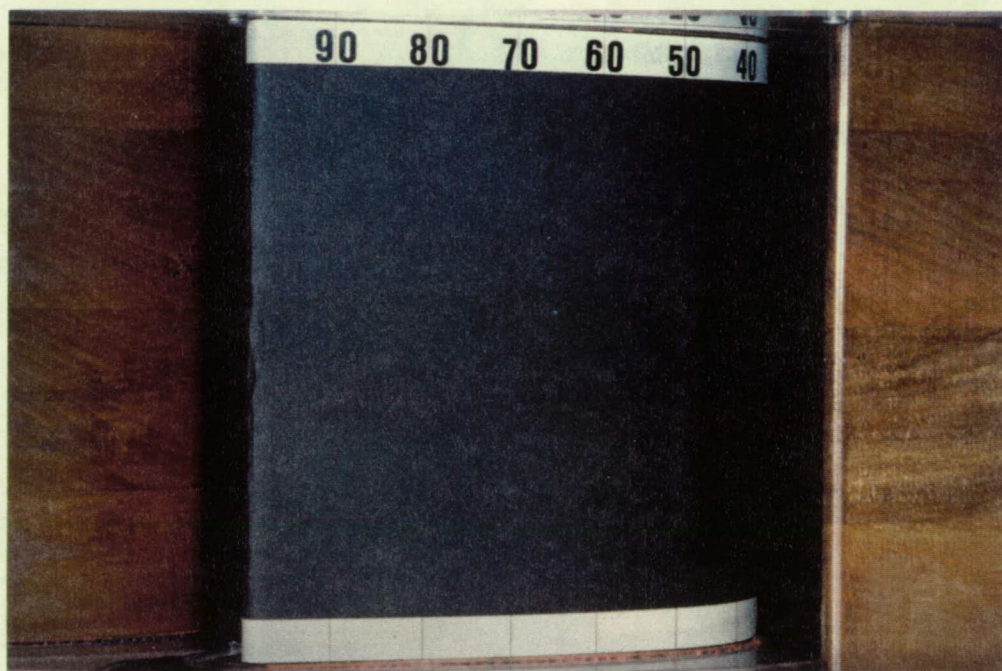


Photo 1

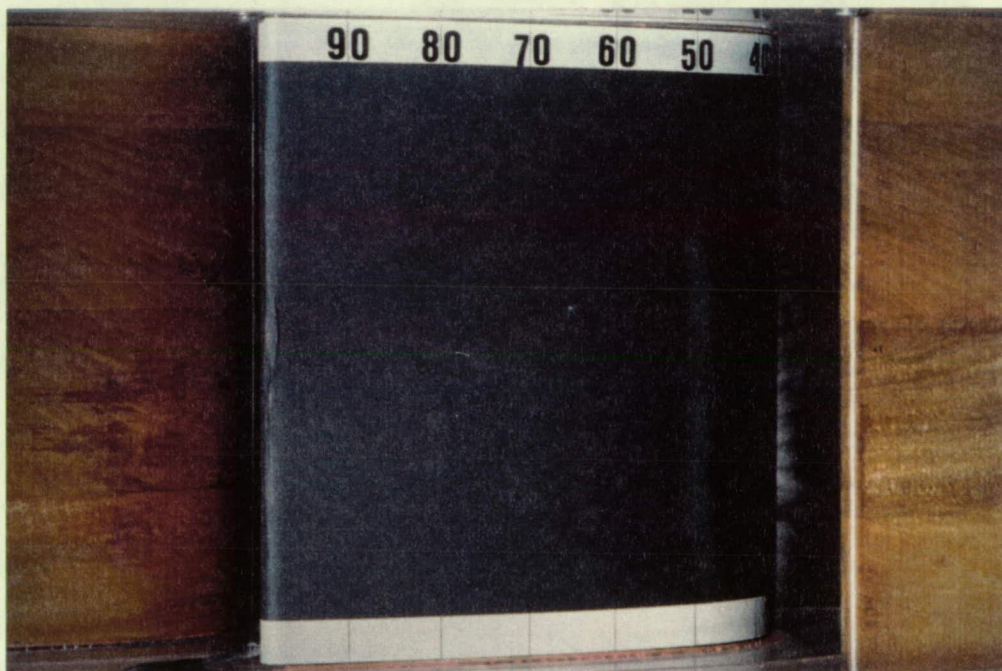


Photo 2

Figure 4.4. Results from the $Re = 330,000$, $Tu = 0.8\%$ test.
a. Trailing edge.

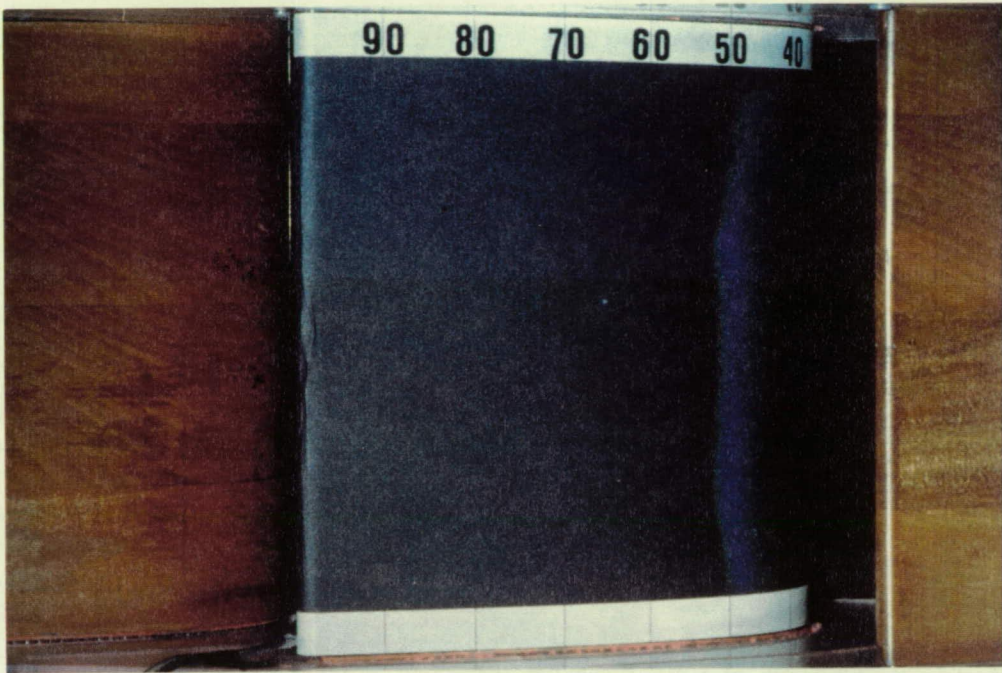


Photo 3

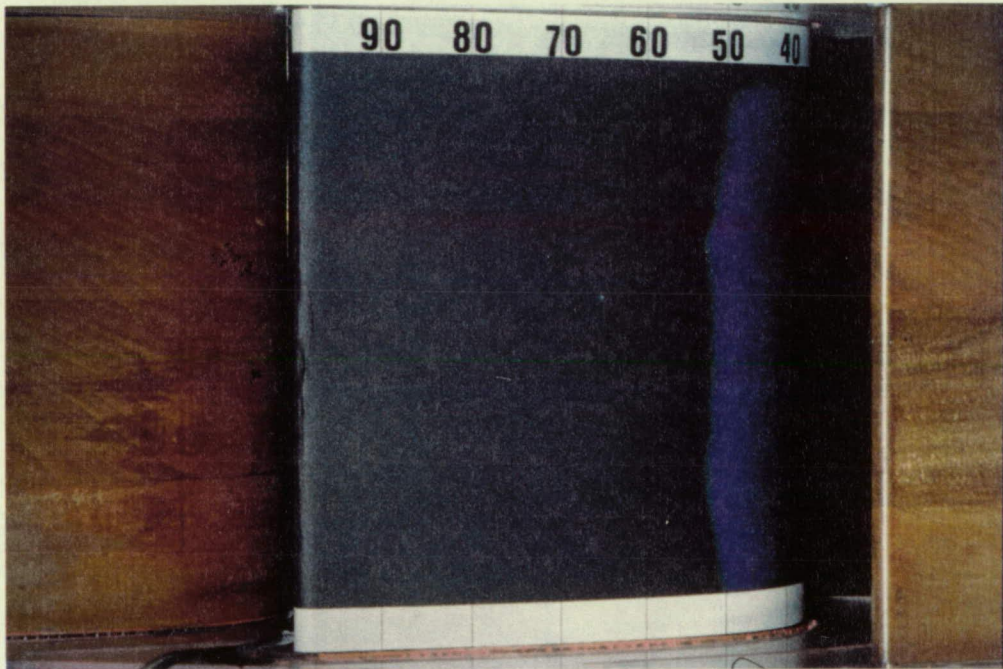


Photo 4

Figure 4.4.a. Continued.

ORIGINAL PAGE
COLOR PHOTOGRAPH

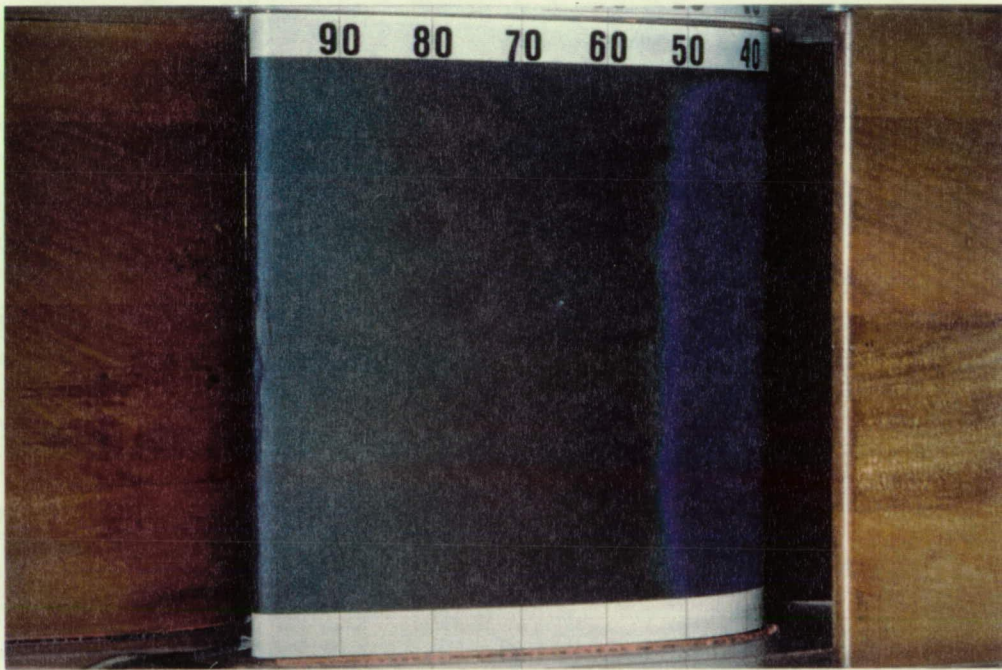


Photo 5

Figure 4.4.a. Continued.

ORIGINAL PAGE
COLOR PHOTOGRAPH



Photo 1

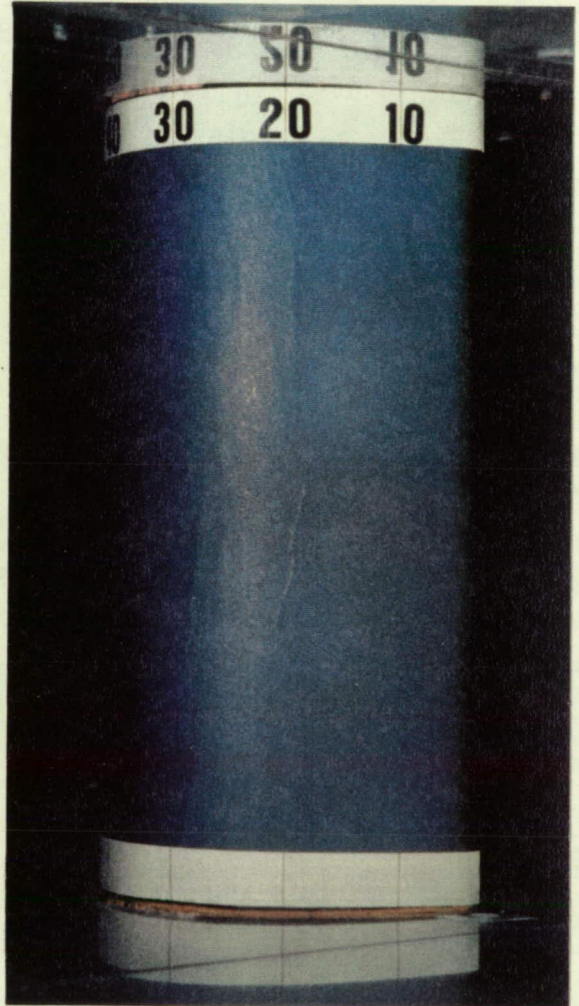


Photo 2

Figure 4.4. Continued.
b. Leading edge.

located at approximately 47% - 50% SSL. This corresponds to the anticipated region of lowest heat-transfer rate at approximately 50% SSL. Photo 2 shows the color play region after an increase in heater power. The colored area is larger and the center of the region is now green. Photo 3 is for a further increase in heater power. The width of the color bands near the leading edge of the bubble around 45% SSL are wider than the color bands near the bubble trailing edge at 53% SSL. This is consistent with the blade temperature curve and indicates an extremely large gradient through the bubble which shows as narrow color bands. The wider color bands near the leading edge of the bubble indicate the more gradual temperature change with distance in this region.

In photo 4 the color bands near the leading edge of the bubble are now almost out of view around the curve of the blade. The region of lowest heat-transfer rate at about 50% SSL has changed to dark blue. The color bands toward the trailing edge of the bubble are very narrow, indicating they are still inside the separation bubble.

In photo 5 the sharp lines are no longer visible, indicating that the color play has moved out of the separation region. The trailing edge is now colored. As seen in the blade temperature curve, the severe temperature gradient moderates at the end of the bubble at 56% SSL. The liquid crystals show this more moderate temperature gradient as wider color bands. The local heat-transfer rate maximum at 60% SSL is visible as regions of faint red.

The leading edge portion of the blade in photo 1 shows the initial color bands beginning in the separation region at 30+% SSL and spreading to approximately 20% SSL. The color bands move evenly from the separation region toward 0% SSL as the heater power is increased. Photo 2 shows that the color bands have advanced to the leading edge and the surface is evenly blue. A large temperature gradient near the stagnation point on the blade near 0% SSL is evident.

This test case was also recorded with a broadcast quality video camera. A prefabricated Hallcrest TLC sheet with the same formulation (R30CIW) was used for the video recording. The color play characteristics of the sheet are the same as for the spray-on coating. The heater and liquid crystal only cover the midspan portion of the blade in the video recording.

Part 1 of the video recording is a series of clips showing liquid crystal color play on the blade surface at discrete heater power settings much the same as for the still photos. Clip 1 shows the initial red color appearing on the blade surface. The power to the heater was increased in increments so that a relatively uniform color change on the blade surface occurred between clips. The trends observed in the still photos hold for the video clips as well. Clips 2 and 3 show the initial region of color expanding and the red turning to green and eventually blue.

Clip 4 shows that the color play is still in the bubble and the color bands near the leading edge of the bubble have moved out of view around the front curve of the blade. Clip 5 shows the

color development beginning on the downstream surface of the blade. The color play inside the separation bubble is now approaching the end of the bubble. In clip 6 the entire trailing surface of the blade is colored. The sharp bands of color are no longer present indicating that the color play is moving out of the bubble. The region of separated flow is now colorless (black).

Part 2 of the video shows the color play on the blade surface as the heater power is continuously increased. No attempt was made to quantify the heater power increase rate. The blade was observed and the heater power increased at a rate that gave a good visual effect. The video sequence starts from the initial appearance of red color on the blade surface. Notice how the sharp color bands in the separation region move slowly toward the trailing edge. However, once color appears on the blade trailing surface, all of the color bands quickly widen and expand across the surface to meet each other. There is a large movement of the color bands in the moderate temperature gradient region near the trailing surface of the blade compared to small movement of the color bands in the separation bubble.

Part 3 is a series of clips at discrete power settings showing the color play on the forward region of the blade. The separation bubble is visible at 30+% SSL. Clips 1 and 2 show the color play moving from the region of the bubble toward the leading edge of the blade. The next series shows the color play during a continuous power increase with no large gradients visible. The color bands sweep from the separation bubble to the blade leading edge.

4.5. $Re = 700,000$, $Tu = 6.4\%$ Case

The $Re = 700,000$ and $Tu = 6.4\%$ case involved natural transition from laminar to turbulent flow with no flow separation. Unlike the previous test case for $Re = 330,000$ and $Tu = 0.8\%$, there were no large temperature gradients on the blade.

Figure 4.5 from Ref. [16] shows selected AC voltage waveforms for this case. Turbulent spots indicating the start of natural transition begin to appear at 31% SSL, sensor location 15. The waveforms indicate transition is complete and fully turbulent flow exists at 55.5% SSL at sensor location 28 and further downstream.

Figure 4.6 shows Halstead, Okiishi, and Wisler's [16] hot-film sensor data for $Re = 700,000$ and $Tu = 6.4\%$. The RMS voltage ratio data show a large magnitude increase beginning at approximately 30% SSL and reaching a peak at 48% SSL. The RMS voltage ratio magnitude falls rapidly after the peak is attained and reaches a steady-state level at 60% SSL. This region of high RMS voltage ratios is characteristic of transition [16].

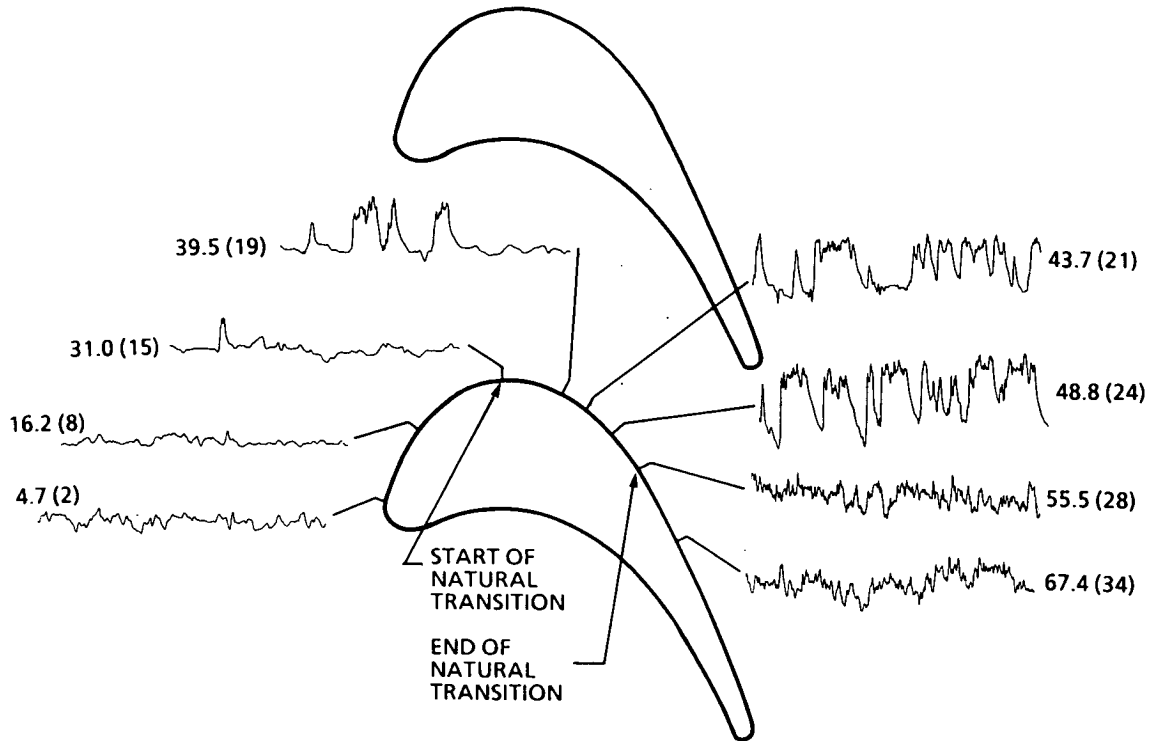


Figure 4.5. Selected AC voltage waveforms for $Re = 700,000$ and $Tu = 6.4\%$.

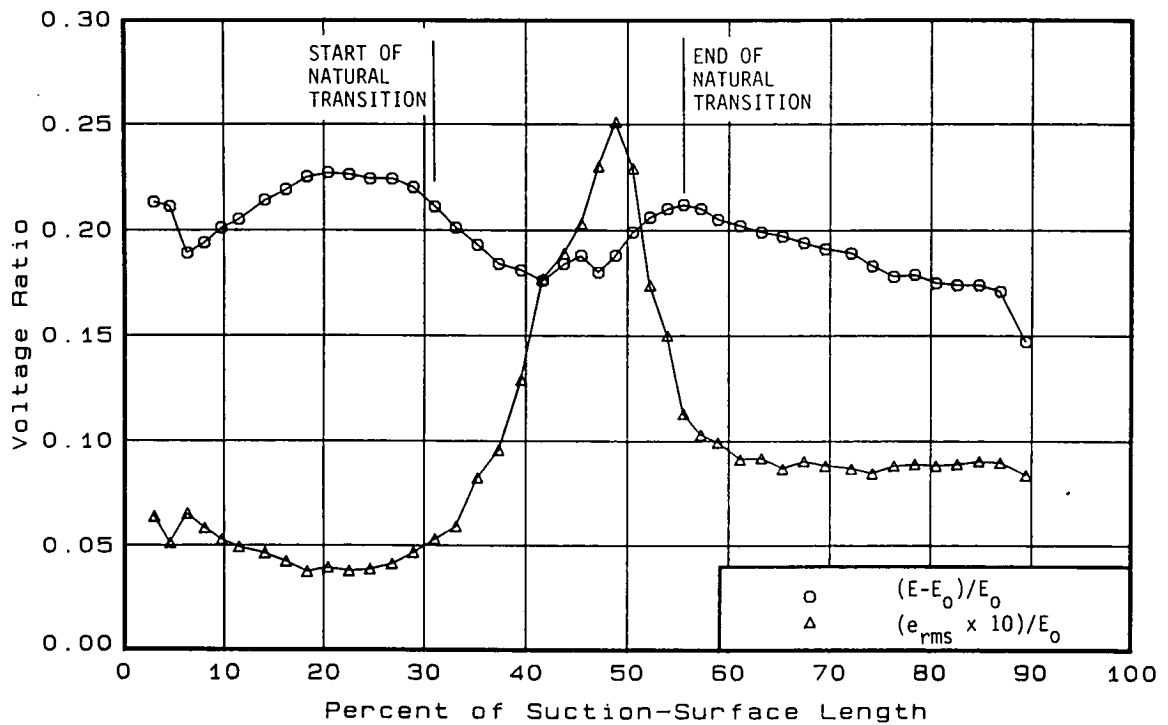


Figure 4.6. DC and RMS voltage output from hot-film sensors for $Re = 700,000$ and $Tu = 6.4\%$.

The DC voltage ratio data go through a broad maximum on the leading edge surface of the blade. The DC voltage ratio data are decreasing at the beginning of natural transition and reach a minimum midway through the transition at 45% SSL. There is a small fluctuation in the curve before the DC voltage ratios increase until the end of transition. The DC voltage ratio data then show a gradual decrease in magnitude to the trailing edge of the blade.

Figure 4.7 shows still photos at discrete heater power settings of a $Re = 770,000$ and $Tu = 6.4\%$ test that used a Hallcrest spray-on liquid crystal coating with the formulation R30CIW. For each photo the power input to the heater was changed so that a relatively uniform color change appeared on the blade. Photo 1 shows the initial color on the blade. Again from inverting the DC voltage ratio curve, the transition region is expected to have the highest surface temperature and lowest blade transfer rate.

In photo 2 the trailing edge region of the blade is a uniform green and the area of transition has turned a dark blue. The end of transition is visible as a band of green mixed with red at around 55% SSL, caused by the higher heat-transfer rate at the end of the natural transition region. The color changes are very gradual on the trailing surface at 60% - 100% SSL, showing the gradual change in blade surface temperature in this area of the blade.

Photos 3 and 4 show the progression of color as the heater power is increased. The blue color band from the trailing edge grows wider and eventually meets the blue regions from the transition. Further power increases turn the crystals dark blue and eventually back to colorless.

Results from the forward surface of the blade were also photographed for this case. The color play is more difficult to see because of the blade curvature and the difficult lighting conditions. Photo 1 shows the initial color on the blade. From the blade temperature curve, there is a local minimum in the blade temperature curve at 20% SSL. As the heater power is increased, photo 2 shows the color changes are broad and gradual. The anticipated local minimum does not appear. A reflection on the blade surface from the lighting also makes the interpretation of the results difficult. Notice the high heat-transfer rate on the leading edge of the blade near the stagnation point. The narrow bands of color in this area indicate the gradient.

The $Re = 700,000$ and $Tu = 5.4\%$ case was also recorded on video tape. A Hallcrest prefabricated TLC sheet (R30CIW) was used for these clips.

The first part of the video is a series of clips showing the liquid crystal color play at discrete heater power settings. Clip 1 shows the initial color play on the blade surface appearing at 40% - 50% SSL. Clip 2 shows the result of a heater power increase. The region of color has expanded and is now blue. There is no other color play showing on the blade.

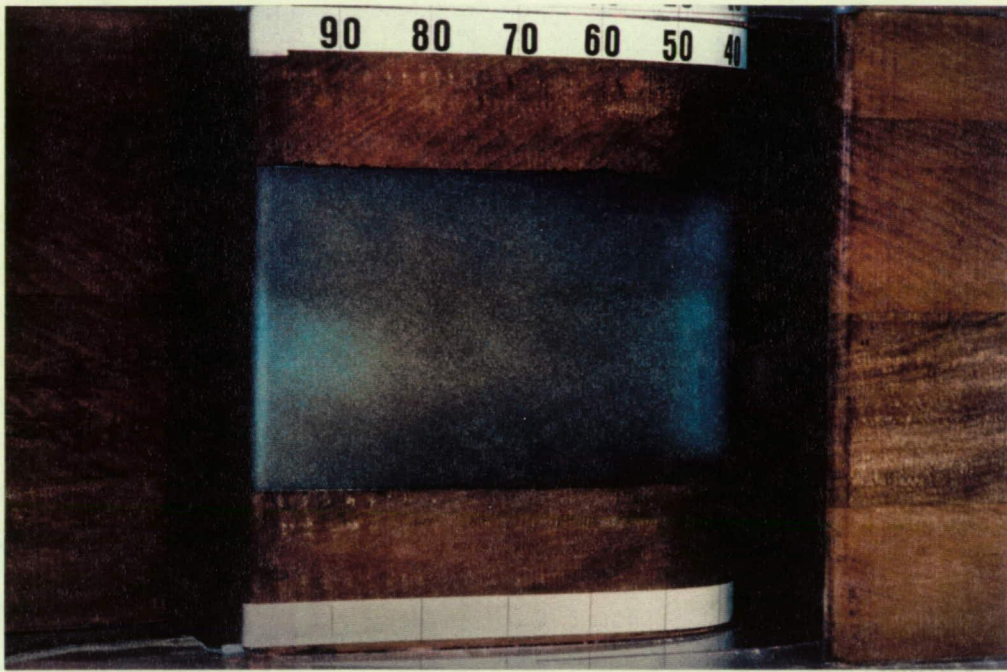


Photo 1

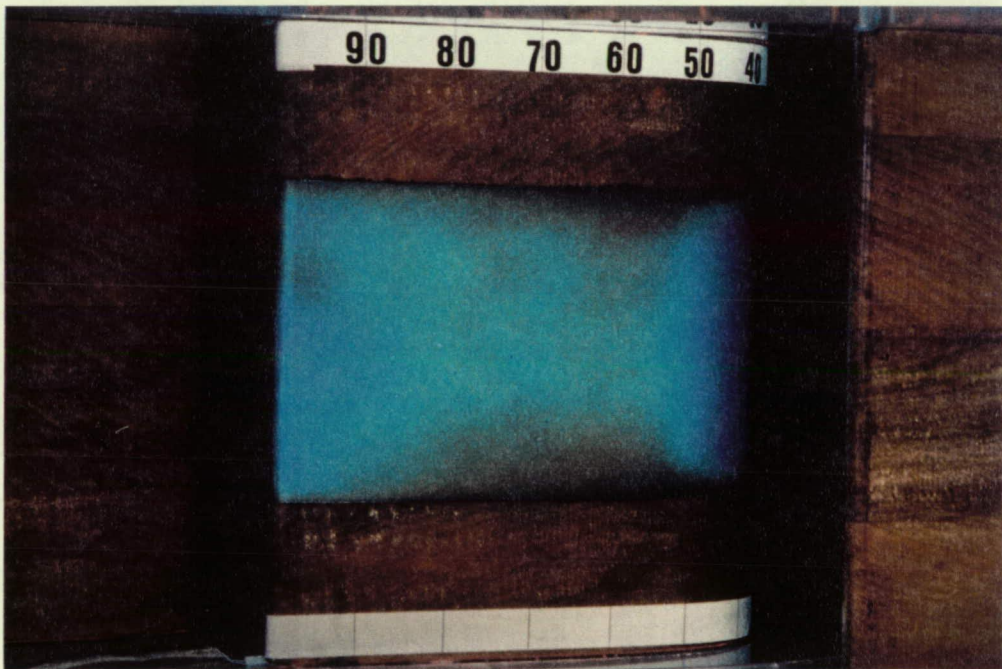


Photo 2

Figure 4.7. Results from the $Re = 700,000$, $Tu = 6.4\%$ case.
a. Trailing edge.

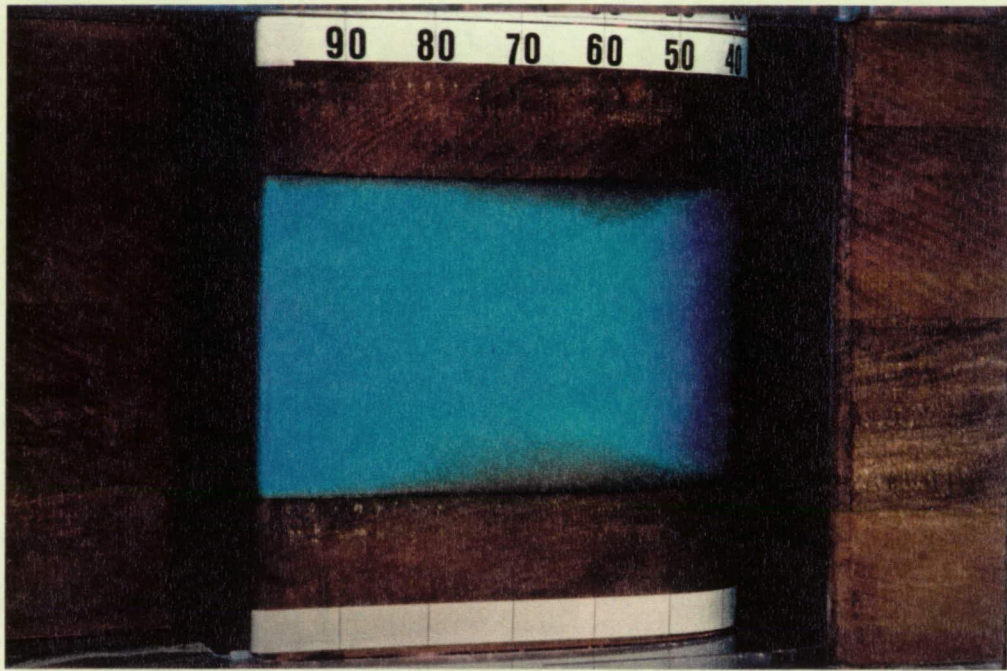


Photo 3

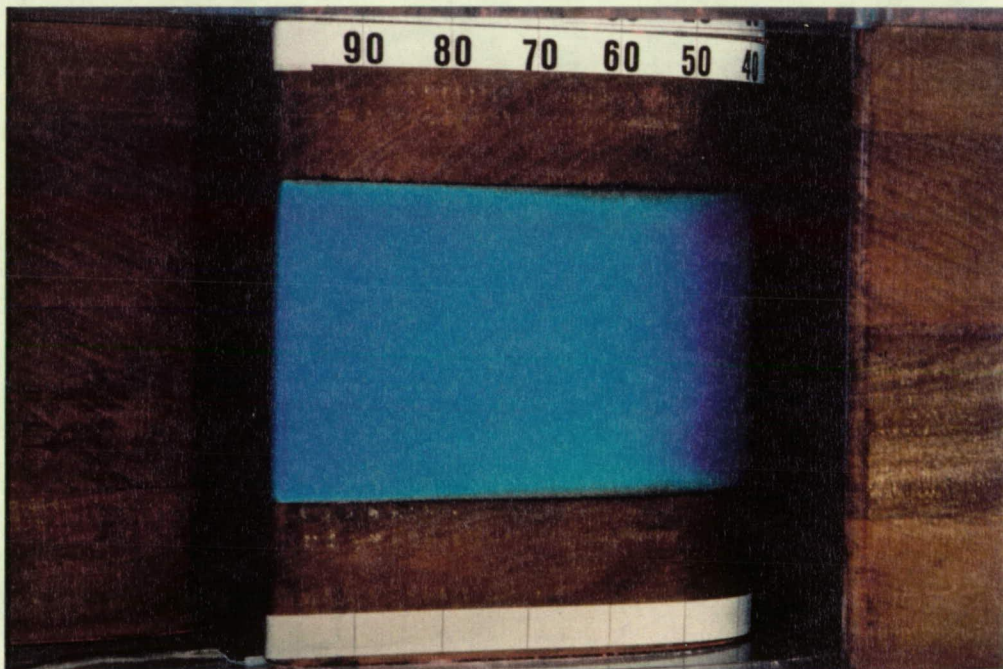


Photo 4

Figure 4.7.a. Continued.

ORIGINAL PAGE
COLOR PHOTOGRAPH

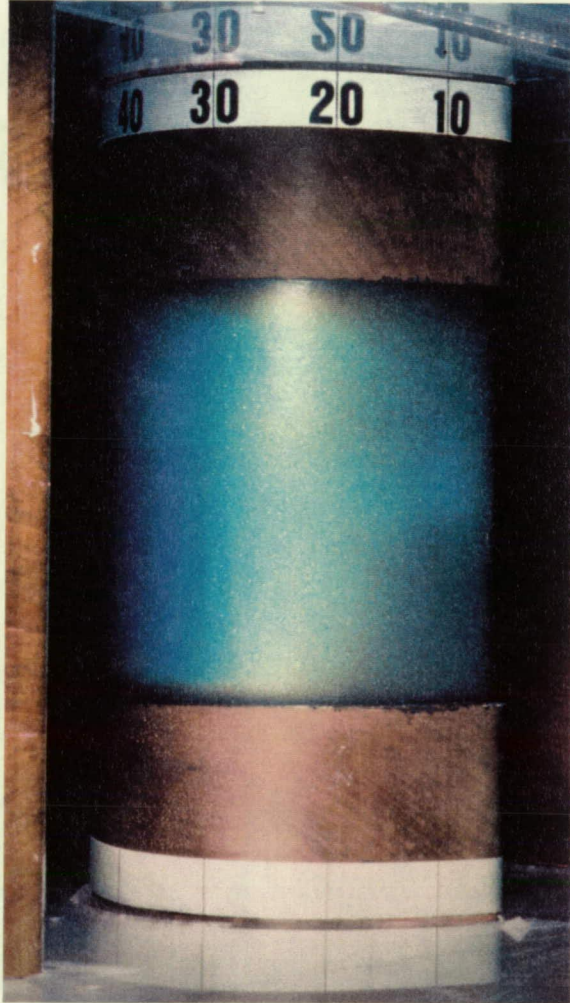


Photo 1

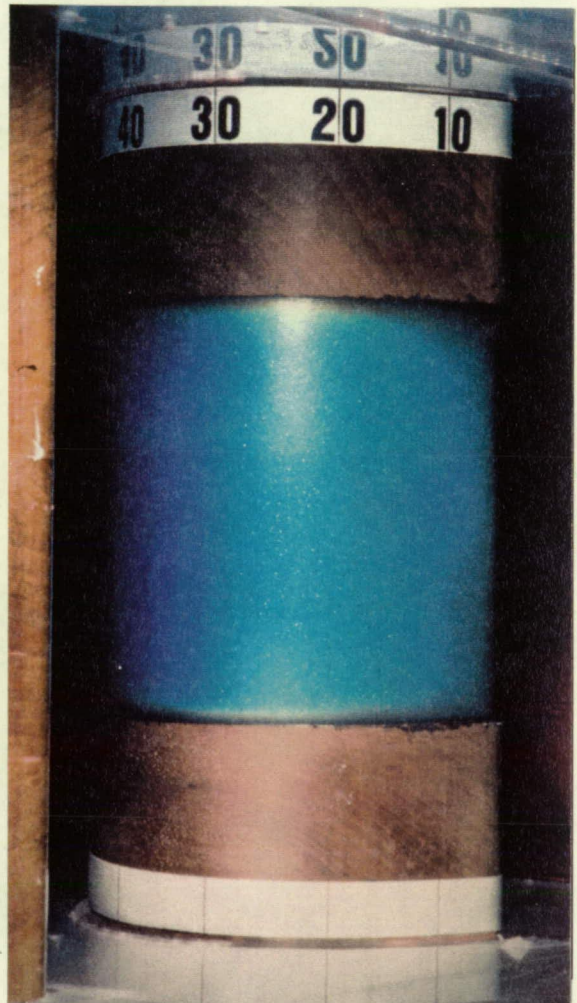


Photo 2

Figure 4.7. Continued.
b. Leading edge.

In clip 3 the transition region is turning dark blue and the trailing edge surface is beginning to color. In clip 4 the trailing edge surface is now turning green. The peak in the heat-transfer rate in the region 55% - 65% SSL is apparent. As the heater power is increased, shown in clip 5, the region of high heat rate remains reddish or green as the trailing edge and transition region of the blade turn dark blue to colorless.

The second section of the video shows the color play during a continuous power increase. Notice the region of higher heat-transfer rate at 55% - 70% SSL.

Color play on the leading edge of the blade was also recorded. The series of clips begins with the initial color red appearing at 30% - 40% SSL (clip 1). As the heater power is increased the color bands move toward the leading edge of the blade. Eventually the heater power is increased enough that the entire leading edge appears uniformly blue (clip 2). The temperature gradient is no longer visible on the surface. The color play during a continuous power increase is shown next. The color bands sweep from the transition region toward the leading edge. Only a shallow gradient is visible.

5. BOUNDARY-LAYER VISUALIZATION USING SHEAR SENSITIVE LIQUID CRYSTALS

Shear sensitive liquid crystals reflect light at a specific wavelength depending on the level of shear stress acting on the crystals. It is possible to correlate different reflected colors with different shear stress levels. A technique was developed to use the shear sensitive properties of these crystals to indicate boundary-layer development on the surface of a turbine blade section. Information from the boundary-layer studies done by Halstead, Okiishi, and Wisler [16] using surface mounted hot-film gages formed the basis for this technique.

Referring to Fig. 4.3, the DC voltage ratio data are proportional to the one-sixth root of the wall shear stress as follows:

$$\frac{E - E_o}{E_o} \propto T_w^{1/6} \quad (5.1)$$

The local wall shear stress, like the heat-transfer rate, varies widely over the blade surface. This variation in wall shear stress results in a variation of the color reflected by the liquid crystal coating. These color variations can be related to the boundary-layer development on the blade.

Preliminary studies involving shear sensitive liquid crystals were accomplished with a kit of four chiral nematic liquid crystal formulations, B-N/74A, B-N/74B, B-N/75A, and B-N/75B, supplied by Hallcrest. These crystals were in an unencapsulated, or neat form, and were responsive to temperature as well as shear stress variations. The four formulations allowed us to set a range of values for the red start and bandwidth of the final mixture by combining varying proportions of the four formulations. For shear stress to dominate over temperature in influencing the color response of the crystals, the anticipated blade surface temperature must fall within the color play bandwidth of the final liquid crystal mixture [17, 18].

When initially applied to the blade surface, the crystals appeared to be colorless or a faint red. When exposed to a light shear stress, the crystals appeared to be red. As the shear level increased, the crystals changed in appearance from red to yellow to green to blue, the same color play sequence associated with temperature-sensitive crystals responding to increasing temperature.

Figure 5.1 shows the color response of a chiral nematic crystal mixture during a test. Endwall suction was not used during this test, and the effects of the end wall boundary layers are evident in the crystal color pattern. The separation region appears as a spanwise oblong dark colored area located at about 50% SSL. Reattachment shows as a curved line in the liquid crystals

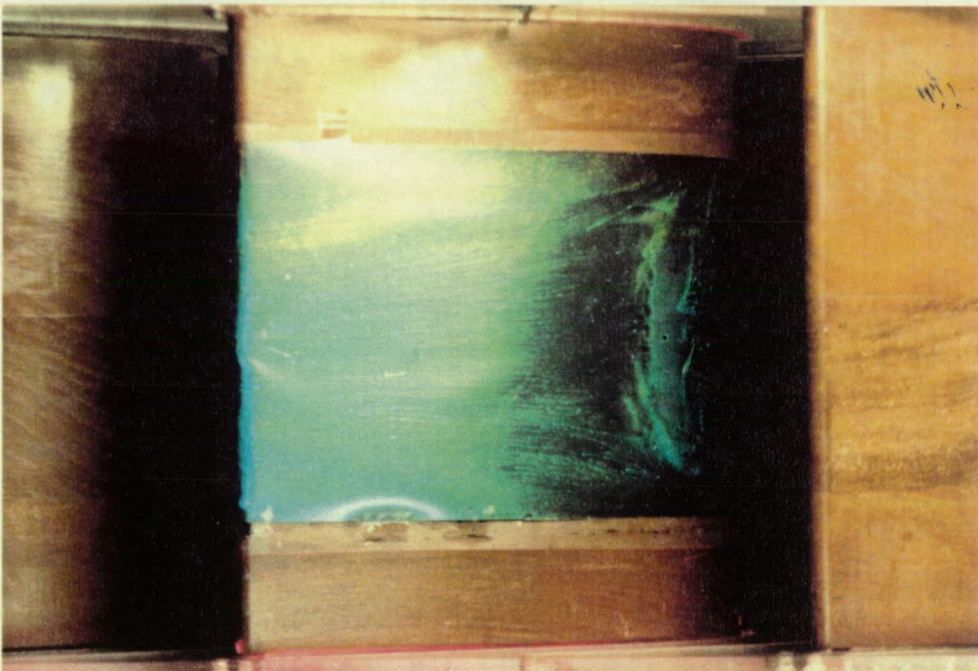
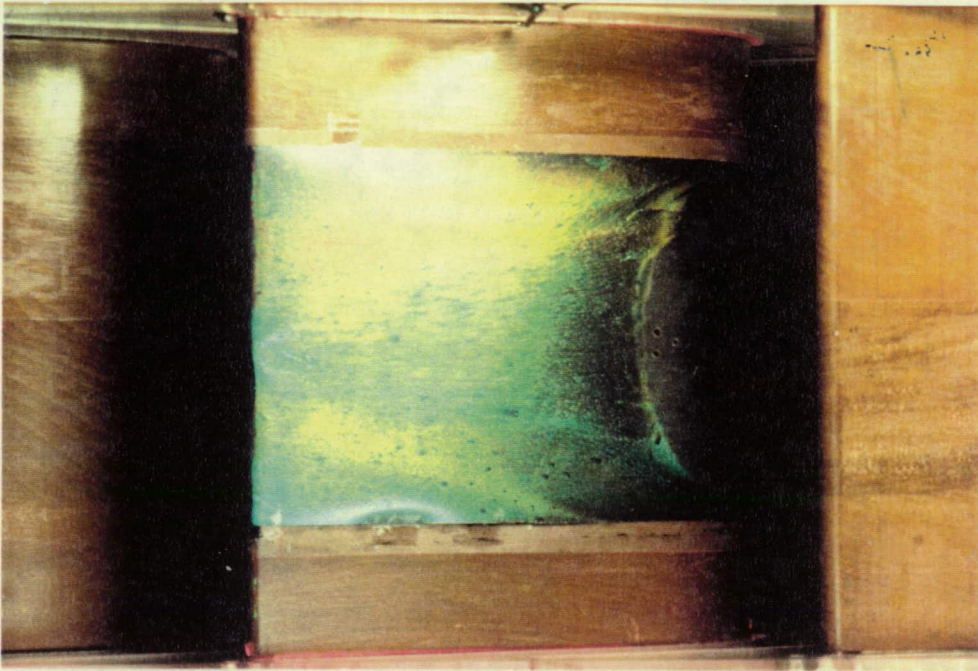


Figure 5.1. Color response of shear sensitive crystals on blade surface with no endwall suction.

that traces the edge of the separation region. This line appears yellow in places and green in others. The color play on the trailing surface of the blade is a mixture of green and yellow with hints of red.

Close observation of the crystal coating in the photos reveals an orange peel pattern caused by the flow near the blade surface. The dark spots and streaks visible were caused by dust particles impacting the surface and causing the crystals to flow.

Results using the original chiral nematic liquid crystal kit were disappointing. Since the crystals often flowed under shear stress on the surface, permanent color patterns resulted. In addition, temperature effects were impossible to separate from shear stress effects. Hallcrest subsequently supplied some other liquid crystal formulations that were shear sensitive but almost unresponsive to temperature variations. Five different samples were evaluated, CN/R2, CN/R3, CN/R45C, BN/R50C and BCN/165. The first three samples were cholesteric crystals; the fourth was a chiral nematic crystal; and the fifth was a mixture of cholesteric and chiral nematic crystals. All samples were in an unencapsulated form. Three of the samples, BCN/165, BN/R50C, and CN/R45C, were low-viscosity crystals while CN/R2 and CN/R3 were higher-viscosity crystals.

Bonnet, Jones, and McDonnell [29] discuss the use of these types of shear sensitive mixtures in their studies of flow visualization and shear measurement in aerodynamic testing. They described the results of their detailed examination of the selective reflection characteristics of their crystals as a function of illumination and viewing angle. More importantly, they reported an improved method for detecting laminar to turbulent transition based on a flow-induced crystal coating texture change from focal-conic to Grandjean.

Surface preparation is critically important for the successful use of shear sensitive crystals. The surface must be free of any solvents or oils to prevent residues that will affect the crystal color play. A flat-black, water-based paint was applied to the surface in a smooth even coat. Oil-base or aerosol paints are not acceptable because of the residues involved. The crystals were applied with an air brush or by using a soft paintbrush. Using a paintbrush worked very well for our application. The crystals could be moved around on the surface with the brush until an even coat of the desired thickness was produced.

The technique for detecting laminar to turbulent transition proposed by Bonnet, Jones, and McDonnell [29] involves observing the crystal coating texture change from the thermodynamically preferred focal-conic texture to the shear-induced Grandjean texture. Figure 5.2 from Ref. [29] shows a representation of the molecular realignment that occurs in the change from focal-conic to Grandjean texture. The focal-conic texture can be formed by solvent action or by heating the crystals. If the solvent/crystal mixture is brushed onto a surface and left undisturbed as the solvent evaporates, the crystals will align themselves in the focal-conic texture. The crystal molecules will

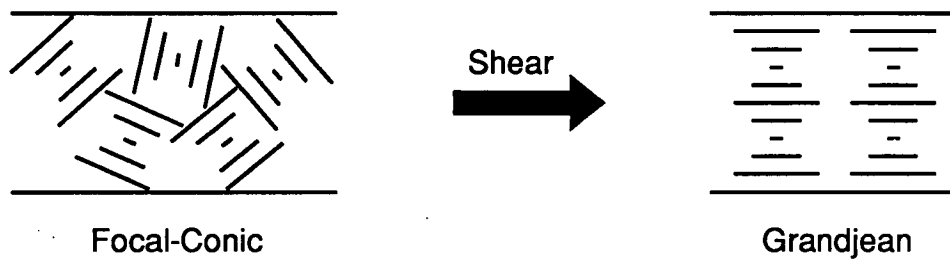


Figure 5.2. Focal-conic and Grandjean liquid crystal textures.

also align themselves in the focal-conic texture if they are heated to a temperature above their clearing point temperature. This is easily done by using a heat gun or an infrared lamp; we used an infrared lamp. Since the focal-conic texture is not optically active, the crystals appear colorless in this form.

The Grandjean texture is an optically active texture and appears bright rusty-red. The crystals can be aligned into this texture by aerodynamic or other shear stresses. For example, brushing the crystals with a soft dry paintbrush will also align them into this texture.

The relative sensitivities to shear stress of the five formulations were determined by using a compressed air nozzle on side-by-side samples of the materials. The shear sensitive crystals displayed a range of the colors: yellow, green, and blue, in response to the shear stress levels generated by the air jet on the coated surface. The BN/R50C was the lowest viscosity formula and also the most responsive to aerodynamic shear. CN/R45C was the next most responsive. Because of the relatively low shear levels present on the turbine cascade blade surface, the BN/R50C material was the most suitable for the present application and was used for all of the blade flow tests described below.

For observing laminar to turbulent transition, the crystals were applied to the blade surface and then aligned into the focal-conic texture by lamp heating. Figure 5.3 shows the crystals on the blade surface in the focal-conic texture. The laminar to turbulent transition was observed both with and without endwall suction at $Re = 540,000$ and $Tu = 0.8\%$. The surface shear stress levels for the flow corresponding to $Re = 330,000$ and $Tu = 0.8\%$ were not high enough to cause a color change in the shear sensitive crystals. According to Halstead, Okiishi, and Wisler [16], the boundary-layer development for lower and higher Reynolds numbers was similar with a laminar separation bubble reattaching with a turbulent flow. As confirmed in Fig. 5.4, a distinct separation and turbulent reattachment is present on the blade surface for $Re = 540,000$. The reattachment occurs at 55% SSL.

Figure 5.5 shows the reattachment and turbulent flow on the blade surface as the red color in the crystals for both cases, with and without endwall suction. The test was run in a transient fashion; the airflow was started and a delay of 15 to 25 seconds occurred as the airflow attained steady-state velocity and the color change occurred. Bonnett, Jones, and McDonnell [29] calibrated their crystals so that the time for color response was related to the shear stress level in their tunnel. Figure 5.6 shows the crystals after stopping the airflow, demonstrating that the color change is permanent. The liquid crystal results agree well with the hot-film sensor results of presented in



Figure 5.3. Crystals on the blade surface in the focal-conic texture.

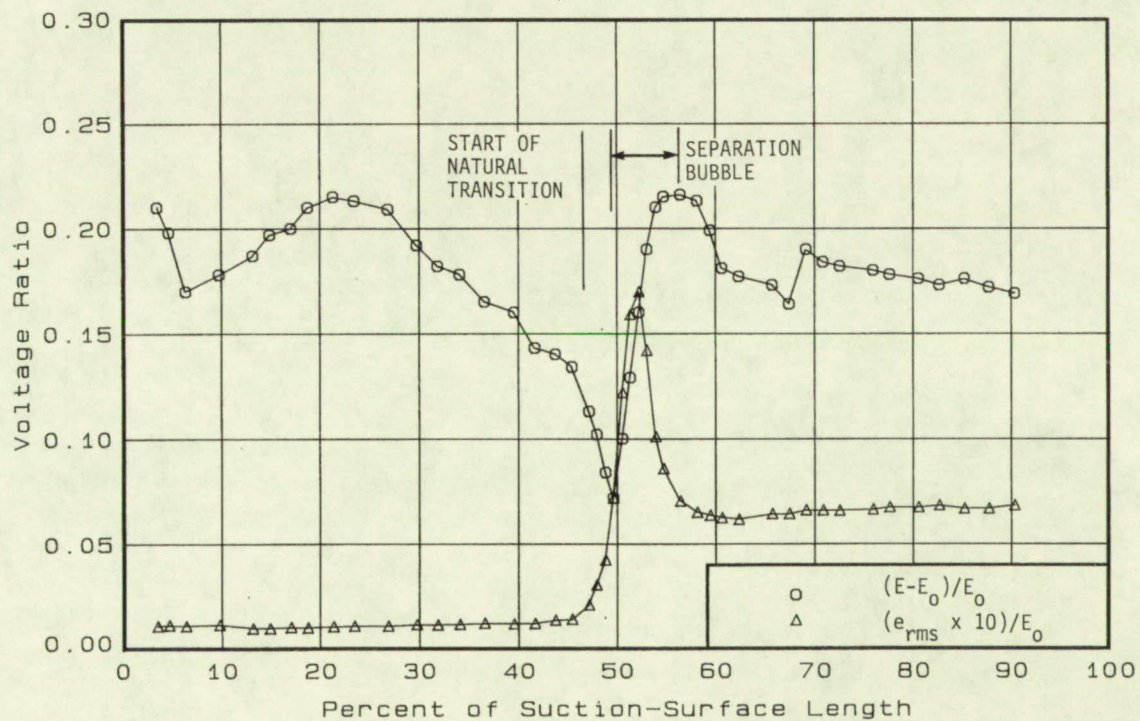
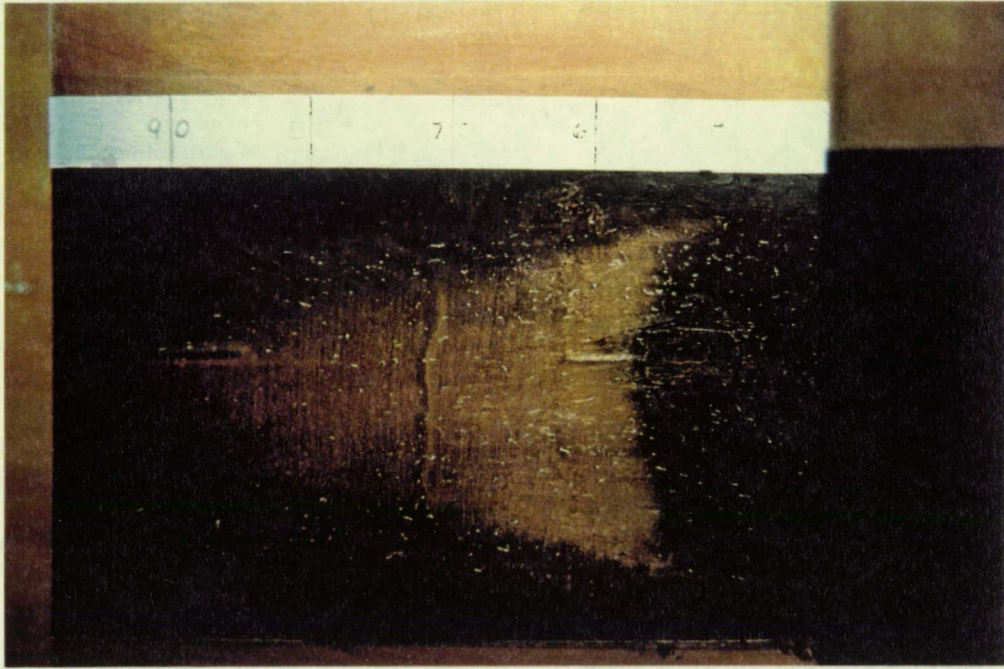
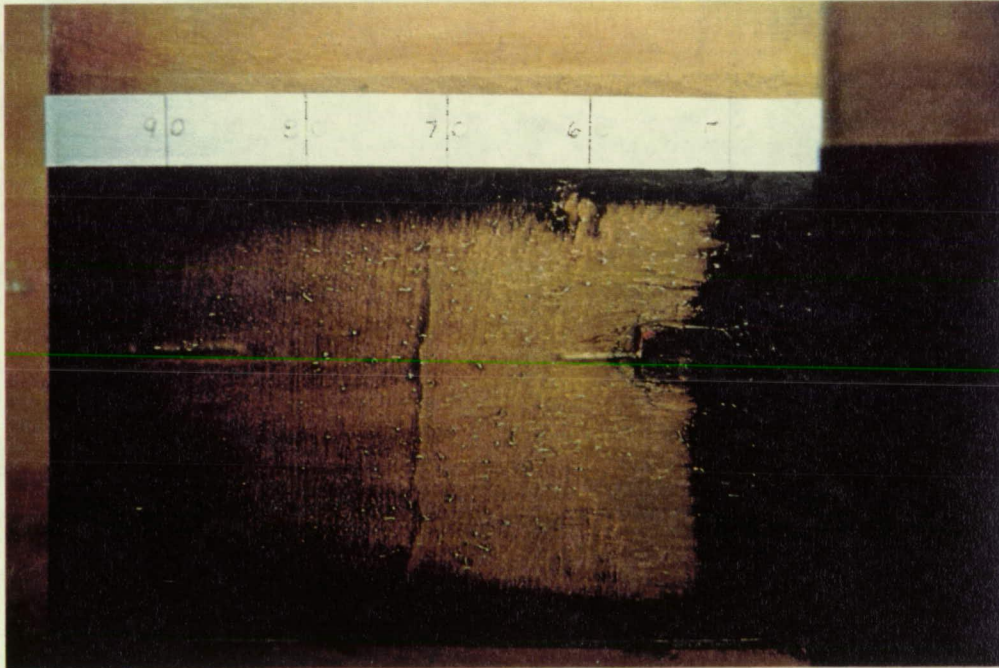


Figure 5.4. DC and RMS voltage output from hot-film sensors for $Re = 540,000$ and $Tu = 0.8\%$ case.

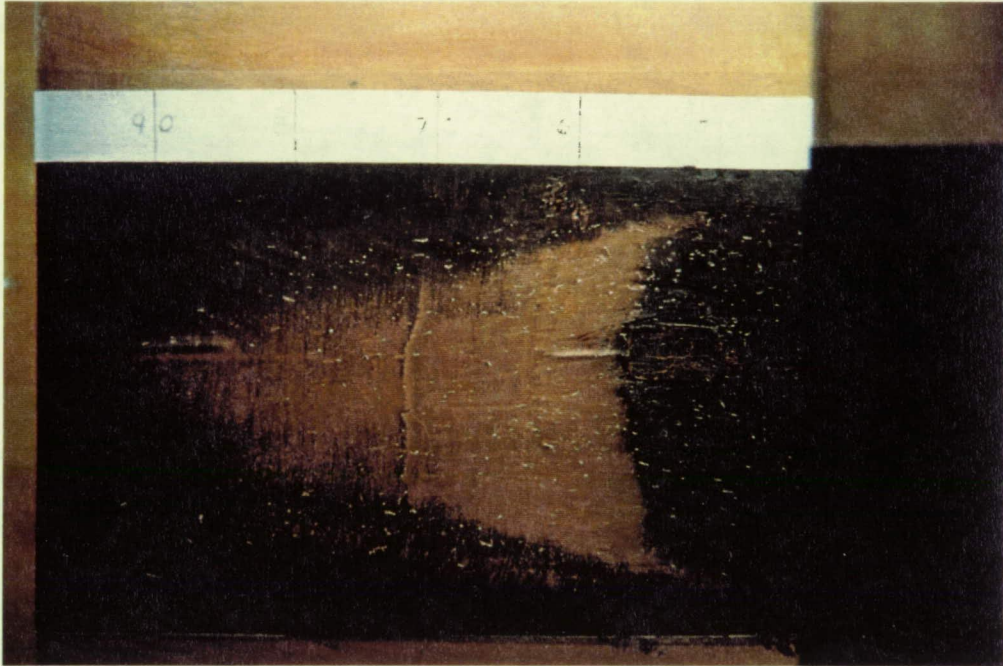


a. No endwall suction.

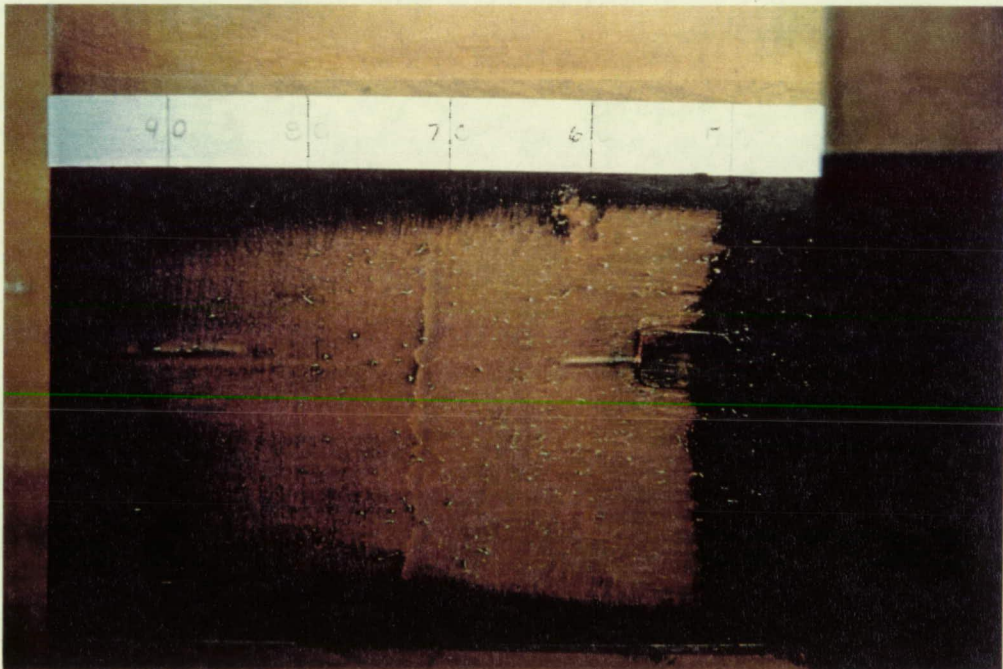


b. With endwall suction.

Figure 5.5. Flow-induced color change showing turbulent reattachment and turbulent flow region.



a. No endwall suction.



b. With endwall suction.

Figure 5.6. Permanent color change due to flow-induced texture change from focal conic to Grandjean.

Ref. [16]. The reattachment line does shift slightly when no endwall suction is used and the three-dimensional character of the flow is readily visible.

The flow reattachment can also be observed by using selective reflection properties of the crystals aligned in their Grandjean texture. The crystals were brushed to align them in the Grandjean texture, Fig. 5.7 and Fig. 5.8. The tunnel was then brought to its steady state condition. The turbulent reattachment and flow region, beginning at approximately 55% SSL, appears red-yellow in Fig. 5.9. This color change is subtle and is difficult to capture on film. The color change is visible at the predicted location and again is shifted in the no endwall suction case. Unsteadiness in the reattachment line and vortices on the trailing surface were visible as color fluctuations in the crystals. The color change from the Grandjean state was not permanent and was reversible. Figure 5.10 shows the crystals with no airflow. The color returned to a deep red over the entire surface. The reattachment and turbulent flow region are still visible because of the different surface texture in this region induced by the turbulent boundary-layer flow.

The results of the shear sensitive crystal tests were also documented on a video recording. The first clip shows the crystals in their focal-conic state, and the next in their Grandjean state. The effects of brushing, which switched the crystals to their Grandjean state, is next demonstrated. Using an infrared lamp to heat the crystals above their clearing point temperature returns them to the focal-conic state. The response of the crystals in their Grandjean state to an air jet is also shown.

The next series of shear sensitive crystal tests shown on the video recording was done with no endwall suction at $Re = 540,000$ and $Tu = 0.8\%$. The laminar to turbulent transition is first indicated by a shear-induced change from focal-conic to the Grandjean texture of the crystals in the turbulent portion of the flow (after flow reattachment). The texture change occurred over a finite time period because of the startup time for the tunnel as well as the crystal response time. Subsequently, with all of the crystals in the Grandjean texture, careful observation reveals a subtle color change beginning at the flow reattachment and turbulent flow transition location.

This series of tests was also performed with endwall suction and recorded with the video camera. The laminar to turbulent transition detection by crystal texture change is again visible. With the crystals all in the Grandjean texture state, the color change with transition is subtle but observable.

In additional tests that were not recorded, shear sensitive liquid crystals were applied to blades of the first rotor row of a low-speed axial-flow research compressor. The compressor was operated at 1500 - 2000 rpm. Using a stroboscope, we observed the crystal coating on the blade surface for any color change as the compressor was throttled and forced into rotating stall. This



Figure 5.7. Crystals on the blade surface in the Grandjean texture.

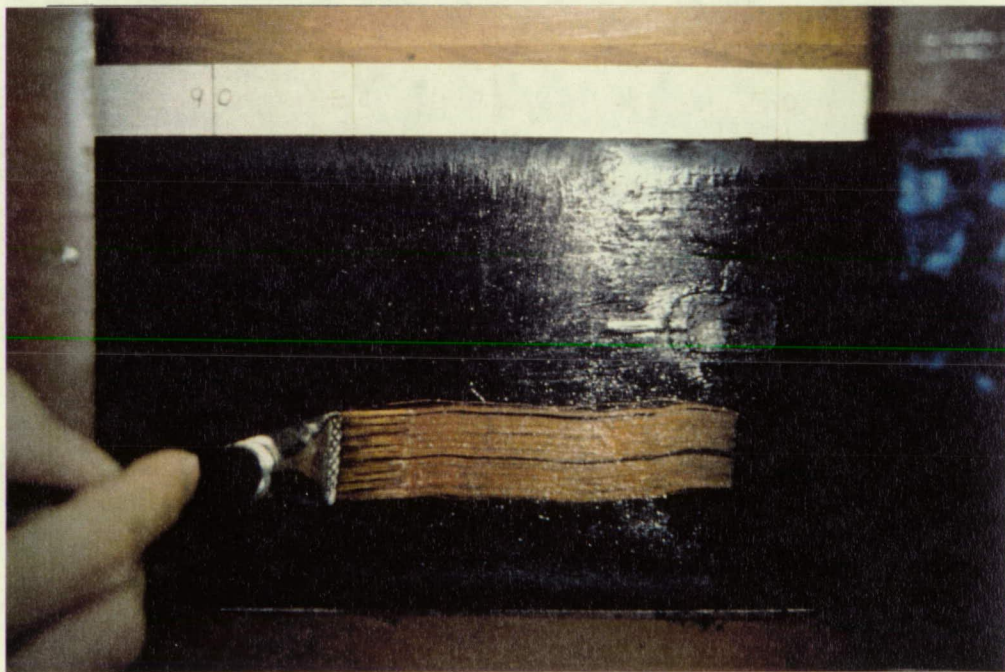
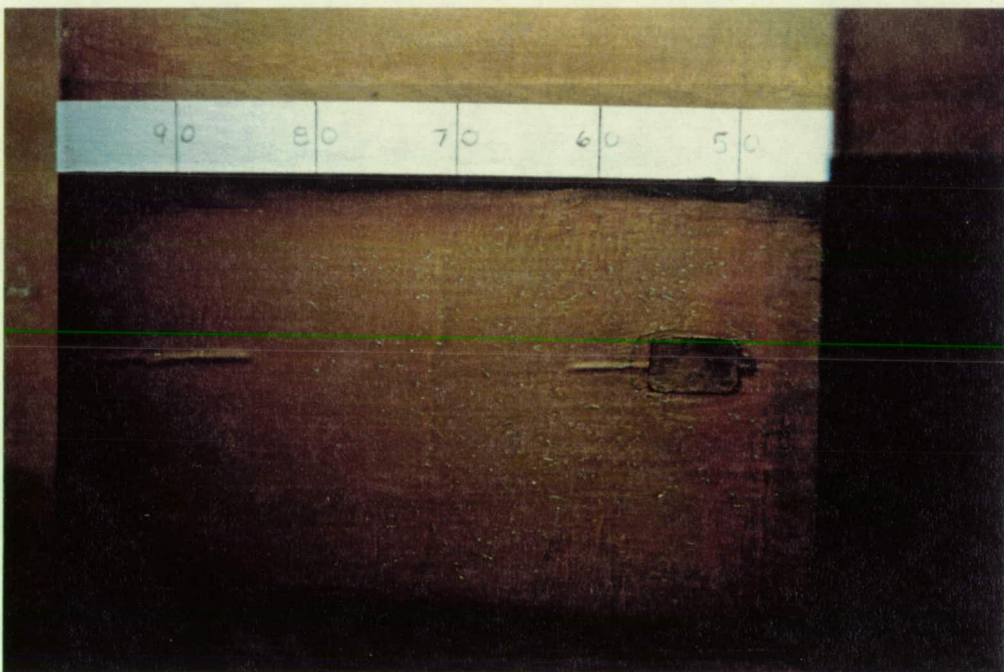


Figure 5.8. Brushing the crystals to obtain Grandjean texture.

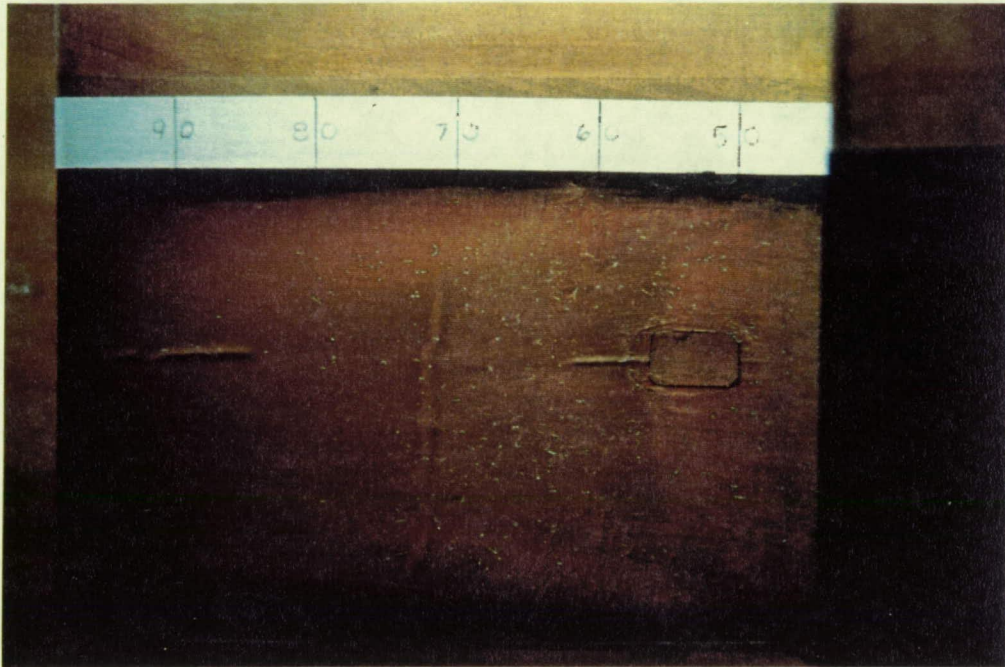


a. No endwall suction.

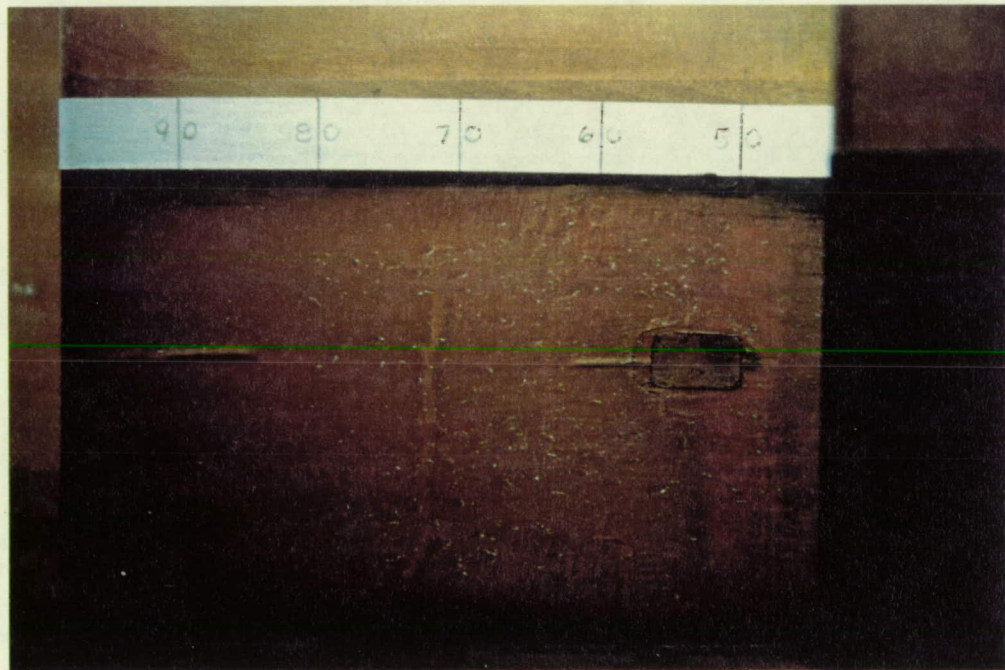


b. With endwall suction.

Figure 5.9. Turbulent reattachment showing as shear-induced color change in the crystals.



a. No endwall suction.



b. With endwall suction.

Figure 5.10. Crystals in Grandjean texture after a test (no airflow).

preliminary investigation did not yield observable results. The shear stress levels on the blade surface were not high enough to cause an observable color change in the crystals because viewing and lighting conditions were not optimum. Centrifugal forces did cause some of the crystal coating to flow off the blade surface; however, sufficient crystal coating remained on the surface so that a crystal color response to shear stress would have been possible.

6. CONCLUSIONS

The results indicate that the combination of a surface heater sheet and a coating of temperature-sensitive liquid crystals provide a suitable method for visualizing the boundary-layer development on a turbine blade surface. The local status of the surface boundary layer on the test turbine blade was known from surface hot-film gage data. Thus, the color patterns seen in the liquid crystal coating on the blade could be interpreted and evaluated. The color patterns observed on the entire blade surface were compared with anticipated color patterns based on the hot-film data. Also, temperature gradients along the flow path were deduced from the color patterns and these gradients compared favorably with anticipated temperature gradients based on hot-film gage data.

With hot-film gage data, we deduced an approximate blade surface temperature curve, with the location of the lowest heat-transfer rate corresponding to the location of the highest surface temperature. The liquid crystal color play confirmed the regions of highest surface temperature. For the $Re = 330,000$, $Tu = 0.8\%$ and $Re = 700,000$, $Tu = 6.4\%$ cases, the regions of highest surface temperature according to liquid crystal colors agreed with those regions indicated by hot-film gage data. For the $Re = 330,000$ case the highest surface temperature region is well defined and easily identified as the start of a separation bubble. The results were much less dramatic for the $Re = 700,000$ case for which natural transition without a separation bubble occurred. The high surface temperature regions identified by liquid crystal results were, however, in the same locations indicated by the hot-film gages, namely in the transition region and at the trailing edge.

Some differences were noted between anticipated results based on the hot-film gage data and observed liquid crystal color patterns on the blade surface. The anticipated response for the blade leading edge, extrapolated from hot-film results, did not correlate well with the observed liquid crystal response there. Further, the color play in different regions of the blade surface was not precisely predictable by observing the conditions in a specific region and using the gage-estimated temperature variation as a means for predicting the appearance of the color play in other regions.

Lack of resolution using liquid crystals may be the reason for these differences between the observed liquid crystal color play and predictions from the hot-film gage data. The large temperature differences associated with separation were easily shown by the liquid crystals. However, the smaller temperature differences due to accelerating or diffusing flow were not resolvable with the bandwidth of the liquid crystals used. Using a narrower color play bandwidth formulation of the liquid crystals may have allowed these more subtle temperature changes to be observed.

Comparing predicted color patterns based on hot-film gage data to actual color patterns observed in the liquid crystals was not an adequate method for observing the actual state of the boundary layer. The absolute color patterns on the blade surface were not a precise indicator of the state of the flow at any one point on the blade compared to another. However, the temperature gradients implied by the color play of the crystals was a better indication of the state of the flow.

The differences in flow-direction temperature gradients on the blade surface for the $Re = 330,000$ case were quite noticeable. The laminar and the turbulent attached flow regions had modest changes in temperature with distance along the blade surface. However, as the separation region was approached, large changes in surface temperature with distance occurred. These steep temperature gradients showed as narrow bands of color in the liquid crystal response and were readily visible.

The large temperature gradients visible in the $Re = 330,000$ case were used to locate the separation bubble region. This was a dramatic example of the large difference in heat-transfer coefficients in the separated and attached laminar and turbulent flows. In the $Re = 700,000$ case, where a marked flow separation did not occur, the color play on the entire blade surface showed as broad bands of color. Although temperature gradients indicated by the color pattern in the liquid crystals were good indicators of flow disturbances such as separation, they were less able to show gradual change phenomenon such as extended transition from laminar to turbulent flow. The determination of laminar or turbulent flow was not possible by observing the temperature response of the liquid crystals.

Both types of coatings, prefabricated sheets and sprayable coatings of temperature sensitive liquid crystals, performed well. The color play was brighter and more vivid with the prefabricated sheets; however, the sheets were more difficult to mount. The spray-on coatings were easy to apply and could be washed off the surface when another coating needed to be applied. The colors in the sprayable coatings were dull and milky and thus the prefabricated sheets were preferred for their color intensity.

Shear sensitive liquid crystals were used to locate the turbulent reattachment and turbulent flow regions on the blade surface for the $Re = 540,000$ and $Tu = 0.8\%$ flow case. Two techniques for using shear sensitive crystals were evaluated. For either technique, the condition of the blackened blade surface was a critical factor. Applying the crystal coating to dry, water-based paint was judged to be the best. The first technique involved the color change associated with a shear induced texture change from focal-conic to Grandjean. The crystals were applied to the blackened blade surface and heated above their clearing point temperature with an infrared lamp to form the focal-conic texture (clear appearance) on cooling. During a test, aerodynamic shear stress

levels above a threshold value aligned the crystals to a Grandjean texture and thus caused a color change from clear to red. The shear stress levels in the turbulent reattachment and turbulent flow regions were sufficient to align the crystals to form a Grandjean texture and the turbulent reattachment was thus located. The color change is not rapid and remains until the crystals are heated beyond their clearing point temperature again.

The second technique for using shear sensitive crystals involved application of the selective reflection properties of the crystals when they were aligned in the Grandjean texture. When a shear stress is applied to the crystals in this state the reflected light undergoes a blue shift. The greater the applied shear stress the larger the blue shift. Under test conditions the turbulent reattachment and turbulent flow regions showed up as yellow colored areas in the crystals. Unsteadiness in the reattachment line and endwall vortices was visible. When the shear stress was removed, the crystals returned to their original color.

There is a minimum shear stress level above which the shear sensitive crystals show a response. Below this shear level, there is no reflected color or texture change. High enough levels of shear will force the crystals to flow on the surface, which causes undesirable inelastic color change patterns in the crystals. Viewing angles and lighting conditions are critical for good results with the shear sensitive crystals. Reflections can be avoided by carefully positioned lighting and viewing. The optimum view angle is perpendicular to the crystal surface. Viewing the crystals from an angle causes a blue shift in the observed color.

The nonintrusive and global visualization attributes of liquid crystal coatings make them desirable for boundary-layer development observation. Shear stress sensitive crystals are especially valuable because they are easy to apply to surfaces and they do not require an auxiliary source of heat. However, the high levels of shear stress required for observable color variations limit the range of application of these crystals.

REFERENCES

1. Hodson, H. P., "Boundary Layer and Loss Measurements on the Rotor of an Axial-Flow Turbine," *ASME Journal of Engineering for Gas Turbines and Power*, 106: 391-399, 1984.
2. Batson, B. W., and Okiishi, T. H., "Comparison of Predicted and Measured Axial Flow Compressor Blade-Section Profile Loss," In *Proceedings of the 1987 Tokyo International Gas Turbine Congress*, Vol. II, Gas Turbine Society of Japan, Tokyo, Japan, 1987.
3. Dring, R. P., Joslyn, H. D., Hardin, L. W., and Wagner, J. H., "Turbine Rotor-Stator Interaction," *ASME Journal of Engineering for Power*, 104: 743-750, 1982.
4. Hodson, H. P., "Boundary-Layer Transition and Separation Near the Leading Edge of a High-Speed Turbine Blade," *ASME Journal of Engineering for Gas Turbines and Power*, 107: 127-134, 1985.
5. Hansen, J. L., and Okiishi, T. H., "Rotor Wake Segment Influence on Stator-Surface Boundary Layer Development in an Axial-Flow Compressor Stage," *AIAA Journal of Propulsion and Power*, 6: 89-94, 1989.
6. Dring, R. P., "Boundary Layer Transition and Separation on a Compressor Rotor Airfoil," *ASME Journal of Engineering for Power*, 104: 251-253, 1982.
7. Evans, R.L., "Boundary Layer Development on an Axial-Flow Compressor Stator Blade," ASME Paper No. 77-GT-11, 1977 .
8. Walker, G. J., "The Unsteady Nature of Boundary Layer Transition on an Axial-Flow Compressor Blade," ASME Paper No. 74-GT-135, 1974.
9. Pucher, P., and Gohl, R., "Experimental Investigation of Boundary Layer Separation with Heated Thin-Film Sensors," *ASME Journal of Turbomachinery*, 109: 303-309, 1987.
10. Hourmaouziadis, J., Buckl, F., and Bergmann, P., "The Development of the Profile Boundary Layer in a Turbine Environment," *ASME Journal of Turbomachinery*, 109: 286-295, 1987.
11. Vijayaraghavan, S. B., and Kavanagh, P., "Investigation of Boundary Layer Transition and Separation in an Axial Turbine Cascade Using Glue-on Hot Film Gages," ASME Paper No. 88-GT-151, 1988.
12. Wisler, D. C., "Loss Reduction in Axial-Flow Compressors Through Low-Speed Model Testing," *ASME Journal of Engineering for Gas Turbines and Power*, 107: 354-363, 1985.
13. Walker, G. J., "Observations of Separated Laminar Flow on Axial Compressor Blading," ASME Paper No. 75-GT-63, 1963.
14. Dring, R. P., Joslyn, H. D., and Hardin, L. W., "An Investigation of Compressor Rotor Aerodynamics," *ASME Journal of Engineering for Power*, 104: 84-96, 1982.

15. Deutsch, S., and Zierke, W. C., "The Measurement of Boundary Layers on a Compressor Blade in Cascade: Part 2—Suction Surface Boundary Layers," *ASME Journal of Turbomachinery*, 110: 138-145, 1988.
16. Halstead, D. E., Okiishi, T. H., and Wisler, D. C., "Boundary-Layer Transition and Separation on a Turbine Blade in a Plane Cascade," AIAA Paper No. 90-2263, July 1990.
17. Gall, P. D., and Holmes, B. J., "Liquid Crystals for High-Altitude In-Flight Boundary Layer Flow Visualization," AIAA Paper No. 86-2592, 1986.
18. Holmes, Bruce J., and Obara Clifford J., "Advances in Flow Visualization Using Liquid-Crystal Coatings," SAE Paper No. 871017, 1987.
19. Collings, Peter J., *Liquid Crystals Nature's Delicate Phase of Matter*, Princeton University Press, Princeton, N. Y., 1990.
20. Parsley, M., "An Introduction to Thermochromic Liquid Crystal Products," Hallcrest Liquid Crystal Division, Nov. 1987.
21. Ferguson, J., "Liquid Crystals," *Scientific American*, 211: 77, Aug. 1964.
22. Klein, Enrique J., Application of Liquid Crystals to Boundary-Layer Flow Visualization, AIAA Paper No. 68-376, 1968.
23. Klein, E. J., and Margozi, A. P., "Exploratory Investigation on the Measurement of Skin Friction by Means of Liquid Crystals," *Israel Journal of Technology*, 7(1-2): 1969.
24. Reda, D. C., "Observations of Dynamic Stall Phenomena on an Oscillating Airfoil With Shear-Stress-Sensitive Liquid Crystals Coatings," 17th ICAS Congress, Stockholm, Sweden, 1990.
25. Hippensteele, S. A., Russell, L. M., and Stepka, F. S., "Evaluation of a Method for Heat Transfer Measurements and Thermal Visualization Using a Composite of a Heater Element and Liquid Crystals," NASA Technical Memorandum 81639, 1981.
26. Hippensteele, S. A., Russell, L.M., and Torres, F.J., "Local Heat Transfer Measurements on a Large, Scale-Model Turbine Blade Airfoil, Using a Composite of a Heater-Element and Liquid Crystals," NASA Technical Memorandum 86900, 1985.
27. Hippensteele, S. A., Russell, L.M., and Torres, F.J., "Use of a Liquid-Crystal, Heater-Element Composite for Quantitative, High-Resolution Heat Transfer Coefficients of a Turbine Airfoil, Including Turbulence and Surface Roughness Effects," NASA Technical Memorandum 87355, May 1987.
28. Jones, T. V., and Hippensteele, S. A., "High-Resolution Heat-Transfer-Coefficient Maps Applicable to Compound-Curve Surfaces Using Liquid Crystals in a Transient Wind Tunnel," NASA Technical Memorandum 89855, 1988.

29. Bonnett, P., Jones, T. V., and McDonnell, D. G., "Shear-Stress Measurement in Aerodynamic Testing Using Cholesteric Liquid Crystals," *Liquid Crystals*, 6(3): 271-280, 1989.